

# Multi-Channel Potts-Based Reconstruction for Multi-Spectral Computed Tomography

Lukas Kiefer<sup>1,2</sup>, Stefania Petra<sup>1</sup>, Martin Storath<sup>3</sup> and Andreas Weinmann<sup>2</sup>

<sup>1</sup> Mathematical Imaging Group, Heidelberg University, Germany

<sup>2</sup> Department of Mathematics and Natural Sciences, University of Applied Sciences Darmstadt, Germany

<sup>3</sup> Department of Applied Natural Sciences and Humanities, University of Applied Sciences Würzburg-Schweinfurt, Germany

**Abstract.** We consider reconstructing multi-channel images from measurements performed by photon-counting and energy-discriminating detectors in the setting of multi-spectral X-ray computed tomography (CT). Our aim is to exploit the strong structural correlation that is known to exist between the channels of multi-spectral CT images. To that end, we adopt the multi-channel Potts prior to jointly reconstruct all channels. This nonconvex prior produces piecewise constant solutions with strongly correlated channels. In particular, edges are strictly enforced to have the same spatial position across channels which is a benefit over TV-based methods whose channel-couplings are typically less strict. We consider the Potts prior in two frameworks: (a) in the context of a variational Potts model, and (b) in a Potts-superiorization approach that perturbs the iterates of a basic iterative least squares solver. We identify an alternating direction method of multipliers (ADMM) approach as well as a Potts-superiorized conjugate gradient method as particularly suitable. In numerical experiments, we compare the Potts prior based approaches to existing TV-type approaches on realistically simulated multi-spectral CT data and obtain improved reconstruction for compound solid bodies.

**Keywords:** multi-spectral computed tomography, image reconstruction, structural regularization, multi-channel Potts prior, superiorization, Potts model, piecewise constant Mumford-Shah model, non-convex optimization, ADMM

## 1. Introduction

We consider the *multi-channel* reconstruction problem which arises in multi-spectral X-ray computed tomography (CT). X-ray imaging entails *polychromatic* X-ray sources, i.e. emitted photons have a spectrum of energies. Conventional energy-integrating CT detectors do not capture different energies. However, there are materials which may not be distinguished from one another in conventional CT as their linear attenuation coefficients (LAC) are nearly equal. Yet, their LAC's might differ when the whole energy spectrum is considered. Thus, such materials may be distinguished, when measurements at multiple energy-levels are available. In this paper we exploit this phenomenon by using *energy-discriminating* photon counting detectors [67].

As in conventional CT, due to acquisition noise, sampling effects and modeling effects, the task of reconstructing volume functions from multi-spectral CT data corresponds to solving an ill-posed inverse problem. This calls for regularization which is often performed by imposing prior structural knowledge on the unknown solution in the form of a penalty called prior function. Typically, the prior function is made part of an energy minimization

model of Tikhonov-type; see, e.g., [62, 46]. In principle, one could apply conventional priors and data models in CT to reconstruct separately each channel of the *multi-channel* images in multi-spectral CT. However, it is well-known that the channel images in multi-spectral CT are strongly correlated: transitions between materials manifest as edges in the channel images and these edges share the *same spatial positions* across the channels. Therefore, an appropriate prior should enforce this spatial correlation of the channels and aid the reconstruction of particularly noise-prone channels on hand of the less problematic channels. To this end, multi-channel extensions of the total variation prior have been proposed [36, 62, 46, 74, 47]. Typically, these TV-type priors enforce inter-channel correlations by imposing higher costs if the edges are not aligned over the channels. However, these priors are essentially based on penalizing the  $\ell_1$ -norm of the channel-wise gradients, and do not necessarily ensure that the resulting boundaries between materials completely align over the channels. Another side-effect of penalizing the  $\ell_1$ -norm of the gradient, is that it leads to contrast reduction, i.e. in the reconstructed image the jump heights between regions with constant intensities are reduced.

In this paper we propose the use of the *Potts prior* for the reconstruction of compound solid bodies from multi-spectral CT measurements. The Potts prior penalizes the length of the jump set of the image, i.e. the support of the gradient as a subset of the domain. As a result, it produces piecewise constant images with sharply localized edges such that the total boundary length of all segments is small. Further, the Potts prior has no contrast diminishing effect [72]. The Potts prior is an established nonconvex regularizer for joint image reconstruction and partitioning as well as for the reconstruction of approximately piecewise constant images given via indirect measurements; see Section 1.1 for a discussion on related work.

Its multi-channel extension –the *multi-channel Potts prior*– has the appealing property that jumps in multiple channels only cost once if they are located in the same spatial position. Therefore, in comparison to TV-type priors, the multi-channel Potts prior produces sharply localized edges which are *strictly* enforced to share spatial positions across channels. The strong channel-coupling provided by the multi-channel Potts prior is especially attractive for multi-spectral CT reconstruction of compound solid bodies. We illustrate this by comparing the multi-channel Potts prior to existing TV-based priors. We note that for piecewise smooth images, as they often appear in medical applications, the use of piecewise smooth Mumford-Shah models is advisable [4, 34, 42]. In the context of smooth signals, the result of the Potts prior may be interpreted as a partitioning of the signal.

Being nonsmooth and nonconvex, the (multi-channel) Potts prior calls for tailored algorithmic approaches. To this end, we consider two approaches based on energy minimization and superiorization, respectively. In particular, we apply the multi-channel Potts prior within the variational *Potts model* (also known as the piecewise constant Mumford-Shah model) and within a new *Potts-based superiorization approach*.

### 1.1. Related Work

We first review work related to multi-spectral CT, followed by work on the Potts model. We conclude with work on superiorization.

*The reconstruction problem and priors in multi-spectral CT.* We start out with related work concerning the reconstruction problem in multi-spectral CT. Kazantsev et al. [46] consider multi-spectral measurements obtained from energy-discriminating photon-counting detectors and propose a prior based on directional total variation (dTV) [6] to exploit structural similarities between channels. The reference channels for dTV are chosen probabilistically in each iteration on the basis of signal-to-noise ratios. The authors compare their method to other existing TV-based approaches by reconstructing the geocore phantom, which we also consider

in our experiments. Toivanen et al. [74] study variational methods for the reconstruction of three channels obtained by sequential measurements following low dose acquisition protocols. In [36], the authors propose an approach of compressive sensing type, where the multi-channel reconstruction is modeled as the sum of a low-rank and a sparse matrix. In [62], the authors use total nuclear variation to regularize the reconstruction and enforce structural correlation between channels. Furthermore, channel-coupling regularizers based on tensor nuclear norms are proposed in [65].

Another interesting problem in multi-spectral CT –apart from the reconstruction problem– is the material decomposition problem. It describes the task of determining the pixel-wise material composition after the multi-channel image has been reconstructed (typically with channel-wise filtered backprojection). Variational approaches to the material decomposition problem were proposed in [54, 32, 31].

*The Potts model.* The Potts prior is often used in the context of energy minimization methods. This class of methods model the result as the minimizer of an energy function that comprises a data fidelity term and a regularizing term. Thereby, the result is close to the available data and it is regularized by enforcing prior knowledge. The Potts prior together with a data fidelity term yields the Potts model. We start with work on the Potts model for directly sensed image data. Originally named after R. Potts due to his work on statistical mechanics [58], Geman and Geman [37] adopted the Potts model for the edge-preserving reconstruction of piecewise constant images and proposed an algorithmic approach based on simulated annealing. The problem was first considered from the viewpoint of variational calculus by Mumford and Shah [55]. Shortly afterwards, Ambrosio and Tortorelli proposed approximations by smooth functionals which are frequently adopted for algorithmic approaches [1]. Other popular algorithmic approaches use active contours [26], graph cuts [12], convex relaxations [57, 25] and the ADMM [71]. We proceed with related work on the Potts model for inverse problems. Existence of minimizers in the inverse setting has been investigated in [33, 34, 60, 45, 72]. Ramlau and Ring proved that, under mild assumptions on the imaging operator and possible function values, the Potts model is a regularizer in the sense of inverse problems [60]. For deconvolution problems, level-set based active contour methods [49] and Ambrosio-Tortorelli type approaches have been proposed [4]. Concerning Radon measurements, Ramlau and Ring propose a method based on active contours [59] and a similar method for SPECT/CT data is proposed in [51, 52]. We note that methods based on active contours have the disadvantage that they require a relatively good guess for the initialization and for the expected number of gray values in the image. In [72], the problem for general imaging operators is approached by an iterative graph cut strategy. We remark that graph cut approaches need to work on a discretized codomain. Therefore, they either need a good guess on the values of the unknown image or a very fine discretization of the codomain which can become very expensive. Another class of approaches is based on solving sequences of surrogate problems [34, 82]. Finally, in [73] the authors propose an ADMM approach. Inspired by this, we adapt ADMM to the multi-spectral CT reconstruction problem, as detailed in Section 4. A thorough treatment of optimization strategies based on the ADMM can be found in [10].

*Superiorization.* The *superiorization methodology* [30, 41] is an alternative to energy minimization approaches. Algorithms emerging from energy minimization approaches typically alternate between a data fidelity step and a regularization step. Superiorization methods also alternate between these two steps as follows: first, one takes an iterative *basic algorithm* that is typically ‘feasibility-seeking’ (i.e. finding some point that is compatible with a family of constraints or an image that complies with the measured projection data) and then investigates its *perturbation resilience* (i.e. whether its termination is still guaranteed

when the iterates are appropriately perturbed). Secondly, one defines a target function which expresses exogenous or prior knowledge of the domain in question. In each iteration, the iterate is perturbed towards a non-ascending direction of this target function. It suffices that this perturbation merely improves on the target function without necessarily minimizing it. The overall process leads to a solution of the basic problem that is superior to the one that would have been reached without the interlaced perturbations (with respect to the target function) without paying a high computational price. The terms “superiorization” and “perturbation resilience” first appeared in [30] and early developments were presented in [13, 14, 15]. Important notions concerning superiorization were introduced in [41]. A condensed introduction to the superiorization methodology and examples can be found in [18]. Superiorization is an active research field [19] and current research can be found in the continually updated bibliography in [17]. Theoretical work is typically concerned with perturbation resilience which lies at the heart of the superiorization methodology [14, 5]. Only few works [20, 22] have addressed the ‘guarantee problem’, that is, a mathematical guarantee that the overall process of the superiorized version of the basic algorithm will not only retain its feasibility-seeking nature but also preserve globally the target function reductions. Similarities between superiorization methods and optimization methods have been studied in [16, 21]. In [40, 89], the (preconditioned) conjugate gradient algorithm is perturbed by non-ascending directions w.r.t. the total variation prior for (single-channel) tomographic image reconstruction problems. Therein, the authors also show theoretical perturbation resilience for the conjugate gradient (CG). In this work, we make extensive use of this property and superiorize CG by a non-convex and non-continuous target function.

### 1.2. Contribution

We investigate reconstruction schemes for multi-spectral CT problems based on the multi-channel Potts prior which enforces strong spatial correlation between the channels. We investigate two approaches. In the first approach, called *Potts ADMM*, we apply the Potts prior within the variational Potts model which leads to a non-convex optimization problem. We adapt the ADMM approach of [73] to the multi-channel reconstruction of multi-spectral CT data. In the second approach, called *Potts S-CG*, we propose a new superiorization approach that perturbs the iterates of the conjugate gradient (CG) method with a block-wise Potts prior as target function towards Potts regularized solutions. As the Potts prior is neither continuous nor convex, existing derivative-based methods for perturbations with TV [89, 21] cannot be employed directly. Consequently, we employ a derivative-free perturbation approach to superiorize CG w.r.t. the Potts prior. We identify Potts ADMM and Potts S-CG as suitable choices for the Potts model and Potts superiorization by comparing the ADMM to a penalty method for the Potts model, and the superiorized CG method to a Landweber iteration. In numerical experiments, we illustrate the benefits of the multi-channel Potts prior in the reconstruction of multi-channel images from multi-spectral CT data. Specifically we compare the proposed Potts ADMM and Potts S-CG to existing TV-type approaches by applying them to realistically simulated multi-spectral CT data. To the authors’ knowledge the Potts prior has neither been considered in the context of multi-spectral CT nor in the context of the superiorization methodology yet.

### 1.3. Organization of the Paper

In Section 2, we briefly explain the measurement process and the forward model in multi-spectral CT. Section 3 explains the (multi-channel) Potts prior and its benefits in

multi-channel image reconstruction. In Section 4, we briefly explain the Potts model and an algorithmic approach based on ADMM. In Section 5, we derive new Potts-based superiorization approaches, which employ the Potts prior to perturb the iterates of the CG method. In Section 6, we compare the Potts ADMM approach and the proposed Potts-based superiorization approach to a penalty method and a Landweber superiorization approach. In Section 7, we apply both methods to image reconstruction from simulated multi-spectral CT data and compare the results to existing methods. In Section 8, we draw conclusions.

## 2. Measurements and Reconstructions in Multi-Spectral CT

### 2.1. The Forward Problem in Multi-Spectral CT

We consider the spectral version of Beer's law

$$I_1(\epsilon) = I_0(\epsilon) \exp\left(\int_{\mathcal{L}} -\hat{u}(z, \epsilon) dz\right), \quad (1)$$

where  $\epsilon$  denotes the energy,  $I_1$  is the spectrum of the X-ray beam incident on the detector,  $z \in \Omega$  denotes the spatial position. Further,  $\hat{u}$  holds the *energy dependent* linear attenuation coefficients that need to be reconstructed and  $I_0$  is the *energy dependent* intensity flux of the X-ray source corresponding to ray  $\mathcal{L}$  from the source to a given detector element.

In the following, we consider  $M$  detectors and assume that the measurements (1) are taken from  $p$  equidistant angles. Thus, a total number of  $m = pM$  discrete measurements are available. Towards a discrete model, we discretize the (unknown) function  $\hat{u}$  on the continuous domain  $\Omega$  which results in a function  $u$  on an  $n \times n$  pixel grid  $\Omega'$ . It is given by

$$u(j, \epsilon) = \sum_{z \in \Omega} \chi_j(z) \hat{u}(z, \epsilon), \quad (2)$$

where  $\chi_j$  denotes the characteristic function corresponding to the pixel  $j \in \Omega'$ . From (1) and for pairs of source-detector positions indexed by  $i$ , we now obtain

$$I_{1,i}(\epsilon) = I_{0,i}(\epsilon) \exp\left(-\sum_{j \in \Omega'} A_{ij} u(j, \epsilon)\right), \quad i = 1, \dots, m, \quad (3)$$

where we denote by

$$A_{ij} := \int_{\mathcal{L}_i} \chi_j(z) dz, \quad i = 1, \dots, m, \quad j \in \Omega', \quad (4)$$

the intersection length of ray  $i$  with pixel  $j$ . (In particular,  $A_{ij} = 0$  if the ray  $i$  does not intersect pixel  $j$ .) We assume that each photon-counting detector acquires the measurements on an interval of energies  $[\epsilon_c, \epsilon_{c+1})$ . Hence, the detectors provide the measurements

$$Y_{i,c} = \int_{\epsilon_c}^{\epsilon_{c+1}} I_{0,i}(\epsilon) \exp\left(-\sum_{j \in \Omega'} A_{ij} u(j, \epsilon)\right) d\epsilon, \quad i = 1, \dots, m, \quad c = 1, \dots, C. \quad (5)$$

After discretizing the energy spectrum with step-size  $\delta > 0$ , we obtain

$$Y_{i,c} \approx \sum_{\epsilon = \epsilon_c, \epsilon_c + \delta, \dots, \epsilon_{c+1} - \delta} I_{0,i}(\epsilon) \exp\left(-\sum_{j \in \Omega'} A_{ij} u(j, \epsilon)\right), \quad i = 1, \dots, m, \quad c = 1, \dots, C. \quad (6)$$

The following simplified measurement model becomes increasingly accurate for fine energy resolutions, i.e., if  $\delta$  is small, [46]:

$$Y_{i,c} \approx I_{0,i}(\epsilon_c) \exp\left(-\sum_{j \in \Omega'} A_{ij} u(j, \epsilon_c)\right), \quad i = 1, \dots, m, c = 1, \dots, C. \quad (7)$$

After taking the logarithm, (7) corresponds to

$$f_{i,c} \approx \sum_{j \in \Omega'} A_{ij} u(j, \epsilon_c), \quad i = 1, \dots, m, c = 1, \dots, C, \quad (8)$$

where we denote  $f_{i,c} = -\log\left(\frac{Y_{i,c}}{I_{0,i}(\epsilon_c)}\right)$ . Towards a compact notation, we let  $f_c \in \mathbb{R}^m$  hold the  $f_{i,c}$  for all rays  $i = 1, \dots, m = pM$  and define the linear operator  $A = (A_{i,j})_{i=1, \dots, m, j \in \Omega'} : \mathbb{R}^{n \times n} \rightarrow \mathbb{R}^m$ , which holds the *ray incidence geometry* of the measurement setup. Hence, we obtain the linear measurement model

$$f_c \approx A u_c \quad (9)$$

for the channels  $c = 1, \dots, C$ .

It is common to assume acquisition noise for photon counting detectors, that is, the measurements are Poisson distributed. Thus, in a setup incorporating noise, the corresponding variant of (7) is given by

$$Y_{i,c} \sim \text{Pois}\left\{I_{0,i}(\epsilon_c) \exp\left(-\sum_{j \in \Omega'} A_{ij} u(j, \epsilon_c)\right)\right\}. \quad (10)$$

As a result, note that  $f_c$  in (9) is not deterministic due to (10). The multi-spectral CT reconstruction problem corresponds to determine  $u_1, \dots, u_C$  from the measurements (9).

*Remark 2.1.* We note that the made assumptions guarantee a measurement model which is linear. This model is frequently used in the literature [39, 36, 65, 62, 46, 74]. We briefly recall its known limitations.

- (i) For coarse energy resolutions, the step between (6) and (7) becomes increasingly inaccurate.
- (ii) We made the implicit assumption that the energy-dependent detection answers in (5) are represented by characteristic functions  $\chi_{[\epsilon_c, \epsilon_{c+1})}$  of the pairwise disjoint intervals  $[\epsilon_c, \epsilon_{c+1})$ . More realistic detector answer functions would not be constant on the corresponding energy spectrum nor would they have disjoint supports.

## 2.2. Reconstruction

In multi-spectral CT, it is common to use model-based reconstruction approaches as a direct inversion of (9) is not feasible due to the present acquisition noise (10), sampling effects, and necessary simplifications in the modeling process. Instead, the reconstruction of  $u$  is usually modeled as the minimizer of an energy function. Typically, such an energy function corresponds to the (weighted) sum of a data term  $\mathcal{D}$  and a regularizer  $\mathcal{R}$ , i.e., the reconstruction is modeled as the solution of a minimization problem of the form

$$\underset{u \in \mathbb{R}^{n \times n \times C}}{\operatorname{argmin}} \sum_{c=1}^C \mathcal{D}(A u_c, f_c) + \gamma \mathcal{R}(u). \quad (11)$$

The data term  $\mathcal{D}$  promotes closeness to the data  $f$  and  $\mathcal{R}$  imposes regularity on  $u$  by penalizing deviations from a priori fixed assumptions on  $u$ . The parameter  $\gamma > 0$  balances the two terms.

*Data term.* Concerning the data term  $\mathcal{D}$ , a natural choice would be based on the log-likelihood associated with the Poisson distribution [66]. However, for non-trivial imaging operators  $A \neq \text{id}$  as in (10), employing such a data term becomes computationally expensive. Thus, it is common for CT reconstruction problems to employ the penalized weighted least squares model (PWLS) instead [31, 46, 65]. The PWLS is a quadratic approximation to the log-likelihood function [64], so that it is computationally more tractable for non-trivial imaging operators. The PWLS is given by

$$\mathcal{D}(Au_c, f_c) = \|Au_c - f_c\|_{W_c}^2 = \|W_c^{\frac{1}{2}} Au_c - W_c^{\frac{1}{2}} f_c\|^2, \quad (12)$$

where each  $W_c \in \mathbb{R}^{m \times m}$  is a diagonal matrix which weighs the measurements within the respective channel. More precisely, the entries of  $W_c$  are chosen as the number of detected photons in the  $c$ -th energy bin (7). (Please note that  $\|\cdot\|$  corresponds to the Frobenius norm, i.e.,  $\|u\|^2 = \sum_{i,j,c} u_{ijc}^2$ .)

*Regularizing term.* In general, an appropriate regularizing term  $\mathcal{R}$  in (11) should enforce prior knowledge on the unknown result  $u$ . For example, compound solid bodies are (approximately) piecewise homogeneous so that an adequate regularizer may enforce piecewise constancy on  $u$ . We note that it is generally assumed that the channels  $u_1, \dots, u_C$  of multi-spectral CT images are strongly correlated [46, 74, 31]. In particular, it was observed that the edges in the channels are spatially correlated, i.e., they are located at the same positions across the channels. As a result, a regularizer  $\mathcal{R}$  in (11) should enforce prior structural knowledge on each channel *as well as* strong correlation between the channels.

In this paper, we propose to use the (multi-channel) Potts prior for  $\mathcal{R}$ , which combines structural knowledge and strong channel correlation as explained in the next section.

### 3. The Potts Prior for Multi-Spectral CT Reconstruction

The Potts prior is an established regularizer for the reconstruction from indirectly given data [59, 60, 52, 50, 73, 82, 48]. In particular, the reconstruction is modeled as the minimizer of an energy functional which consists of the Potts prior and some data term. The thereby obtained model is called the *Potts model* (sometimes also referred to as piecewise constant Mumford-Shah model). We point out that, under mild assumptions, the Potts model is a regularizer in the sense of inverse problems [60].

We start out by describing the Potts prior for single-channel image recovery. Subsequently, we discuss its extension to multi-channel images and explain how this multi-channel Potts prior enforces strong correlation between channels. This property is especially beneficial when dealing with multi-spectral CT data since the edges in different energy channels are generally assumed to be strongly spatially correlated.

#### 3.1. The Single-Channel Potts Prior

In the following, we let  $\hat{u} : \Omega \rightarrow \mathbb{R}$  be an image defined on the rectangular domain  $\Omega \subset \mathbb{R}^2$ . We denote the *Potts prior* by the symbol  $\|\nabla \hat{u}\|_0$ . Formally,  $\|\nabla \hat{u}\|_0$  measures the length of the support of the (distributional) gradient of  $\hat{u}$ , i.e.,

$$\|\nabla \hat{u}\|_0 = \text{length}(\{x \in \Omega : \nabla \hat{u}(x) \neq 0\}), \quad (13)$$

where length is understood w.r.t. the one-dimensional Hausdorff measure. To fix ideas, for a piecewise constant image  $\hat{u}$  with sufficiently regular discontinuity set, the Potts prior (13)



measures the total arc length of this discontinuity set. An important observation is that  $\|\nabla \hat{u}\|_0$  is finite if and only if the image  $\hat{u}$  is *piecewise constant*, so that the results exhibit crisp boundaries which are sharply localized.

Frequently, the Potts prior is replaced by the total variation prior which is given by  $\|\nabla \hat{u}\|_1$  [63]. Using the TV prior typically corresponds to solving convex problems, while using the Potts prior typically leads to nonconvex problems. Hence, the TV prior is theoretically and algorithmically easier to access than the Potts prior. However, the results of TV often lack sharply localized boundaries in situations with limited-data [27, 28] and it can lead to contrast reduction [72]. Furthermore, as a piecewise constant image directly corresponds to a partitioning, the Potts prior may also be used for joint reconstruction and partitioning. Joint approaches typically yield better results than executing these steps successively [52, 59, 60, 73].

In practice, data are discrete and we consider images  $u : \Omega' \rightarrow \mathbb{R}$  on a lattice  $\Omega' = \{1, \dots, n\} \times \{1, \dots, n\}$ . A common discretization of the gradient in (13) is given in terms of finite differences [23, 24, 71] via

$$\|\nabla \hat{u}\|_0 \approx \sum_{s=1}^S \omega_s \|\nabla_{d_s} u\|_0, \quad (14)$$

where  $\|\nabla_{d_s} u\|_0 = |\{x \in \Omega : x + d_s \in \Omega, u(x) \neq u(x + d_s)\}|$  counts the number of intensity changes of  $u$  in the direction  $d_s \in \mathbb{Z}^2$  weighted by  $\omega_s > 0$ . Consequently, the  $\ell_0$ -terms on the righthand side of (14) promote sparsity in the number of intensity changes of  $u$ . The simplest choice of directions are the unit vectors  $d_1 = (1, 0)^T$ ,  $d_2 = (0, 1)^T$  together with unit weights  $\omega_{1,2} = 1$ . This neighborhood system, however, can lead to results which suffer from geometrical staircasing [71]: artificial block artifacts may be introduced to account for edges in the image to be reconstructed which are not parallel to the coordinate axes. This can be improved upon by including the diagonal directions  $d_3 = (1, 1)^T$ ,  $d_4 = (1, -1)^T$  and using the weights  $\omega_{1,2} = \sqrt{2} - 1$ ,  $\omega_{3,4} = 1 - \frac{\sqrt{2}}{2}$ ; for details see [24, 11, 71]. Because of the improved quality, we will use this system of directions and weights throughout the rest of the paper if not stated otherwise.

### 3.2. The Multi-Channel Potts Prior

In the following, we give an extended description of the multi-channel version of the Potts prior (13) which has been previously used for regularizing given color and multispectral images; see, e.e., [71]. To this end, we start with a multi-channel image  $\hat{u} : \Omega \rightarrow \mathbb{R}^C$  with codimension  $C \in \mathbb{N}$ . The  $c$ -th component function of  $\hat{u}$  is denoted by  $\hat{u}_c$ . Further, we denote the (distributional) Jacobian of  $\hat{u}$  analogously to the single-channel case by  $\nabla \hat{u}$ . Similarly to the Potts prior for  $C = 1$  (13), the Potts prior for multi-channel images is given by the length of the support of the (distributional) Jacobian, i.e.,

$$\|\nabla \hat{u}\|_0 = \text{length}(\{x \in \Omega : \nabla \hat{u}(x) \neq 0\}), \quad (15)$$

where the length is understood as in (13). The discrete counterpart of (15) for the function  $u : \Omega \rightarrow \mathbb{R}^C$  on the lattice  $\Omega = \{1, \dots, n\} \times \{1, \dots, n\}$  is now given by

$$\|\nabla \hat{u}\|_0 \approx \sum_{s=1}^S \omega_s \|\nabla_{d_s} u\|_0, \quad (16)$$



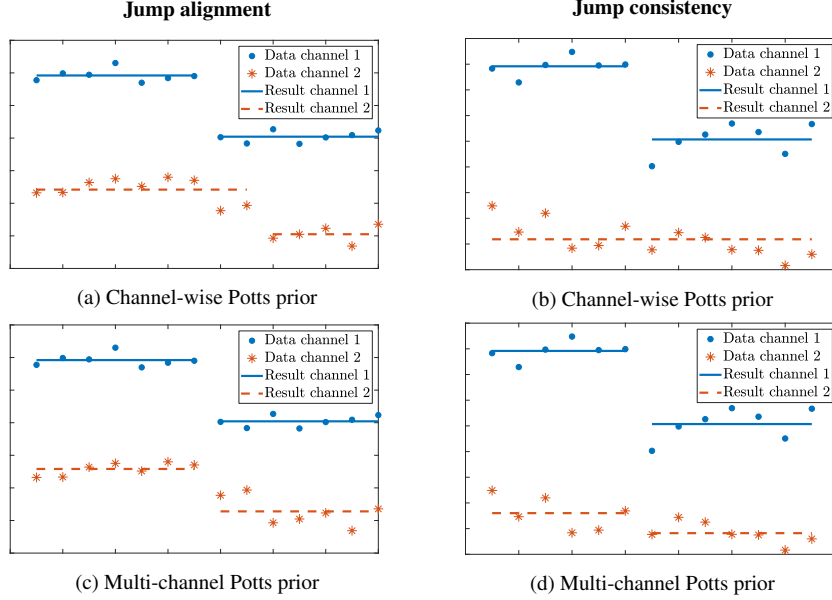


Figure 1: Channel-coupling with the multi-channel Potts prior. *First column:* (a) the channel-wise Potts prior tends to produce jumps at shifted positions in the channels. (c) The multi-channel Potts prior enforces the jumps to be spatially aligned across channels (called the *jump alignment* property of the multi-channel Potts prior). *Second column:* (b) the channel-wise Potts prior may open jumps in a single channel only. (d) The jumps produced by the multi-channel Potts prior are typically present in all channels. Hence, the multi-channel Potts prior provides *jump consistency*.

where the righthand side counts the number of finite difference vectors which are not fully zero, i.e.,

$$\|\nabla_{d_s} u\|_0 = \left| \left\{ x \in \Omega : x + d_s \in \Omega, u_c(x) \neq u_c(x + d_s) \text{ for at least one } c \in \{1, \dots, C\} \right\} \right|. \quad (17)$$

The integer vectors  $d_s \in \mathbb{Z}^2$  and weights  $\omega_s > 0$  have the same role as in the single-channel case (14). In respect of (17), the costs of the multi-channel Potts prior for a jump between  $x$  and  $x + d_s$  in all channels are the same as for opening a jump in a single channel only. On the one hand, this enforces potential jumps at close positions to be spatially aligned across channels in view of the lower costs compared with multiple jumps in different channels (*jump alignment*). On the other hand, jumps are always introduced for all channels simultaneously as a higher closeness to the data can be ensured (*jump consistency*). Thus, the edges of multi-channel images regularized by the multi-channel Potts prior are spatially aligned across all channels, or, in other words, the spatial locations of the channel-wise edges of the produced image are enforced to be completely correlated. In Figure 1, we illustrate the jump alignment and the jump consistency provided by the multi-channel Potts prior by comparing it to the channel-wise Potts prior for dual-channel one-dimensional data.

In the following two sections, we work out two approaches to the numerical reconstruction of piecewise constant multi-channel volume functions by means of the (multi-channel) Potts prior. Firstly, we describe the variational Potts model, which corresponds to a minimization problem of the form (11) with the Potts prior as the regularizer  $\mathcal{R}$ . We approach the Potts model numerically with the ADMM scheme of [73]. Secondly, we derive a new approach based on the Potts prior, which is *not* of the form (11), i.e., it is not based

on an energy minimization model. Rather, we use the Potts prior to *superiorize* an existing iterative solver for (weighted) least squares problems – the conjugate gradient algorithm (CG). In particular, the Potts prior is viewed as a target function which *perturbs* the iterations of CG towards Potts superiorized results.

#### 4. Potts-Based ADMM

The *Potts model* for the (linear) forward operator  $A : \mathbb{R}^{n \times n} \rightarrow \mathbb{R}^m$  and multi-spectral data  $f \in \mathbb{R}^{m \times C}$  is given by the following minimization problem

$$u^* = \operatorname{argmin}_{u: \Omega \rightarrow \mathbb{R}^C} \sum_{c=1}^C \mathcal{D}(Au_c, f_c) + \gamma \sum_{s=1}^S \omega_s \|\nabla_{d_s} u\|_0. \quad (18)$$

Here,  $\mathcal{D}$  stands for the PWLS data fidelity term (12). The nonnegative parameter  $\gamma$  balances the data fidelity and the Potts prior. It is worth considering the limit cases of  $\gamma$ : for  $\gamma \rightarrow 0$  the minimizer of (18) has minimal data fidelity and no regularization takes places. For  $\gamma \rightarrow \infty$  the minimizer of (18) will be a constant function (with minimal data fidelity). It is well-known that the Potts problem (18) is non-smooth, non-convex and NP-hard [77, 12, 82].

*Algorithmic approach with the ADMM.* To obtain good (approximate) solutions of the Potts model (18), we follow the approach first presented in [71] and extended to inverse problems in [73], which is based on the ADMM. The ADMM has been successfully applied to non-convex problems [86, 29, 42, 88, 83]. Contributions from the analytical side are [80, 43, 53, 78, 79]. We note that the ADMM performs particularly well in the context of imaging problems [38, 56, 69, 10, 87]. We briefly recall the scheme for the reader's convenience and provide the necessary adaptations to multi-spectral CT.

As a first step, we recast (18) as a constrained problem. To this end, we introduce splitting variables  $u_1, \dots, u_S$  (each corresponding to a direction  $d_s$  of the discrete gradient) and the variable  $v$  (corresponding to the data term) under the restriction that these new variables are equal to not alter the original problem (18). Hence, we consider the constrained problem

$$\begin{aligned} \min_{v, u_1, \dots, u_S} \quad & \sum_{c=1}^C \mathcal{D}(Av_c, f_c) + \sum_{s=1}^S \gamma \omega_s \|\nabla_{d_s} u_s\|_0 \\ \text{subject to} \quad & u_s - u_t = 0 \text{ for all } 1 \leq s < t \leq S, \\ & v - u_s = 0 \text{ for all } s = 1, \dots, S, \end{aligned} \quad (19)$$

where  $v_c$  refers to the  $c$ -th channel of  $v$ . It is a basic but important observation that we did not alter the original problem, i.e., (18) and (19) are equivalent. The ADMM approach requires to form the augmented Lagrangian of (19), that is,

$$\begin{aligned} \mathcal{L}_{\mu, \rho}(v, \{u_s\}, \{\lambda_{s,t}\}, \{\tau_s\}) = & \sum_{c=1}^C \mathcal{D}(Av_c, f_c) \\ & + \sum_{s=1}^S \left\{ \gamma \omega_s \|\nabla_{d_s} u_s\|_0 + \frac{\rho}{2} \|v - u_s + \frac{\tau_s}{\rho}\|^2 - \frac{1}{2\rho} \|\tau_s\|^2 + \sum_{t=s+1}^S \left\| u_s - u_t + \frac{\lambda_{s,t}}{\mu} \right\|^2 - \frac{1}{2\mu} \|\lambda_{s,t}\|^2 \right\}. \end{aligned} \quad (20)$$

The constraints in (19) are now part of the functional in the form of the corresponding squared deviations weighted by the nonnegative parameters  $\mu, \rho$ . The variables  $\lambda_{s,t}, \tau_s \in \mathbb{R}^{n \times n \times C}$  are the corresponding Lagrange multipliers.

**Algorithm 4.1:** Potts ADMM

---

**Input:** Forward operator  $A \in \mathbb{R}^{m \times n^2}$ , multi-spectral sinogram  $f \in \mathbb{R}^{m \times c}$ , PWLS weights  $W \in \mathbb{R}^{m \times m \times C}$ , stopping parameter  $\text{tol} > 0$ , jump penalty  $\gamma > 0$

**Output:**  $u^* \in \mathbb{R}^{n \times n \times C}$

- 1 Initialize  $v^0, u_1^0, \dots, u_S^0, \lambda_{s,t}^0, \tau_s^0$  by zero.
- 2  $k \leftarrow 0$
- 3 **repeat**
  - /\* Solve the channel-wise PWLS problems \*/
  - 4  $v^{k+1} = \operatorname{argmin}_v \|Av - f\|_{W_c}^2 + \frac{\mu_k S}{2} \left\| v - \frac{1}{S} \sum_{s=1}^S \left( u_s^k - \frac{\tau_s^k}{\rho_k} \right) \right\|^2$  \*
  - /\* Solve linewise Potts problems along the directions  $d_s$  \*/
  - 5 **for**  $s = 1, \dots, S$  **do**
  - 6  $w_s^k = \frac{\rho_k v_k + \tau_s^k + \sum_{t=s+1}^S (\mu_k u_t^k - \lambda_{s,t}^k) + \sum_{r=1}^{s-1} (\mu_k u_r^{k+1} + \lambda_{r,s}^k)}{\rho_k + \mu_k(S-1)}$
  - 7  $u_s^{k+1} = \operatorname{argmin}_{u_s} \frac{2\gamma\omega_s}{\rho_k + \mu(S-1)} \|\nabla_{d_s} u_s\|_0 + \|u_s - w_s^k\|^2$
  - 8 **end**
  - /\* Update the multipliers \*/
  - 9  $\lambda_{s,t}^{k+1} = \lambda_{s,t}^k + \mu_k(u_s^{k+1} - u_t^{k+1})$  for all  $s \neq t$  \*
  - 10  $\tau_s^{k+1} = \tau_s^k + \rho_k(v^{k+1} - u_s^{k+1})$  for all  $s$
  - /\* Increase the coupling parameters \*/
  - 11  $\mu_k \leftarrow \mu_{k+1}, v_k \leftarrow v_{k+1}$  \*
  - 12  $k \leftarrow k + 1$
- 13 **until**  $\|u_s^k - u_{s+1}^k\|_\infty < \text{tol}$  for all  $s = 1, \dots, S-1$  and  $\|u_s^k - v^k\|_\infty < \text{tol}$  for all  $s$ ;
- 14 **return**  $u^* = \frac{1}{S} \sum_{s=1}^S u_s^k$

---

In each ADMM iteration, the Lagrangian  $\mathcal{L}$  is sequentially minimized w.r.t.  $v$  and  $u_1, \dots, u_S$  and afterwards a gradient ascent step is performed on the multipliers. After some algebraic manipulation (see [Appendix A.1](#)), the minimization of the Lagrangian w.r.t. the data variable  $v$  reads

$$\operatorname{argmin}_v \mathcal{L}_{\mu,\rho} = \operatorname{argmin}_v \sum_{c=1}^C \mathcal{D}(Av_c, f_c) + \frac{\mu S}{2} \left\| v - \frac{1}{S} \sum_{s=1}^S \left( u_s - \frac{\tau_s}{\rho} \right) \right\|^2 \quad (21)$$

and the minimization of the Lagrangian w.r.t.  $u_s$  is given by

$$\operatorname{argmin}_{u_s} \mathcal{L}_{\mu,\rho} = \operatorname{argmin}_{u_s} \frac{2\gamma\omega_s}{\rho + \mu(S-1)} \|\nabla_{d_s} u_s\|_0 + \left\| u_s - \frac{\rho v + \tau_s + \sum_{t=s+1}^S (\mu u_t - \lambda_{s,t}) + \sum_{r=1}^{s-1} (\mu u_r + \lambda_{r,s})}{\rho + \mu(S-1)} \right\|^2. \quad (22)$$

We elaborate on efficiently solving (21)-(22) in the subsequent paragraph. As it is common when dealing with non-convex problems, we employ monotonically increasing sequences  $(\mu_k)_{k \in \mathbb{N}}, (\rho_k)_{k \in \mathbb{N}}$  as coupling parameters. This allows the splitting variables to develop rather independently in the first iterations and forces them to become equal in the later iterations. We summarize the ADMM scheme for the multi-channel Potts model (18) in [Algorithm 4.1](#).

*Solving the subproblems in the ADMM scheme.* The crucial observation is that the subproblems (21) and (22) can be solved efficiently. We start with the first subproblem (21). For arbitrary data  $f, z \in \mathbb{R}^{n \times n \times C}$  and  $\mu > 0$  it is given by

$$v^* = \operatorname{argmin}_{v \in \mathbb{R}^{n \times n \times C}} \sum_{c=1}^C \|W^{\frac{1}{2}} A v_c - W^{\frac{1}{2}} f_c\|^2 + \frac{\mu}{2} \|v - z\|^2. \quad (23)$$

The  $\ell_2$ -regularized problem (23) can be solved for each channel  $c$  separately and the unique minimizer  $v^*$  is channel-wise determined by the weighted normal equations

$$\left(A^T W_c A + \frac{\mu}{2} I\right) v_c^* = A^T W_c f_c + \mu z_c. \quad (24)$$

(Note that  $I$  denotes the identity.) Thus, solving (23) corresponds to solving the linear system (24) for each  $c = 1, \dots, C$ . We use the conjugate-gradient method to solve (24).

The remaining subproblems (22) in  $u_1, \dots, u_S$  have the generic form

$$\operatorname{argmin}_{u_s \in \mathbb{R}^{n \times n \times C}} \|u_s - f\|^2 + \gamma \|\nabla_{d_s} u_s\|_0 \quad (25)$$

for some data  $f \in \mathbb{R}^{n \times n \times C}$  and  $\gamma > 0$ . We note that solutions of (25) are not necessarily unique. However, the set of data for which the solution is non-unique is a zero-set in  $\mathbb{R}^n$  [85]. Since only one direction  $d_s$  of the discretized gradient is involved, (25) decomposes into one-dimensional (vector-valued) Potts problems along the paths induced by the direction  $d_s$ ; see Figure 2 for an illustration of these paths. We obtain a minimizer of (25) by determining the minimizers of each of these one-dimensional Potts problems separately. This corresponds to minimizing functionals of the following type

$$P(u) = \|u - g\|^2 + \gamma \|\nabla u\|_0. \quad (26)$$

Here,  $u, g \in \mathbb{R}^{C \times n}$  and the  $\ell_0$ -term denotes the number of jumps of  $u$ , i.e.,

$$\|\nabla u\|_0 = \left| \{i \in \{1, \dots, n-1\} : u_c(i) \neq u_c(i+1) \text{ for at least one } c\} \right|. \quad (27)$$

Despite being a non-convex problem, we use the well-known fact that the one-dimensional Potts problem (26) can be solved non-iteratively and exactly by dynamic programming [8, 9, 3, 84, 44, 35] which we briefly describe in the following. Further details can be found in [35, 70]. Assume that we have computed the minimizers  $u^l$  of (26) for reduced data  $(g_1, \dots, g_l) \in \mathbb{R}^{C \times l}$  for each  $l = 1, \dots, r, r < n$ . Then the minimum value of (26) for data  $(g_1, \dots, g_{r+1})$  is given by

$$P(u^{r+1}) = \min_{l=1, \dots, r+1} P^*(u^l) + \gamma + \mathcal{E}^{l:r+1}, \quad (28)$$

where we define  $u^0$  to be the empty vector, let  $P(u^0) = -\gamma$  and denote by  $\mathcal{E}^{l:r+1}$  the sum of the quadratic deviations of  $(g_l, \dots, g_{r+1})$  from its channel-wise means. If we denote the minimizing argument of (28) by  $l^*$ , the minimizer  $u^{r+1}$  is given by

$$u^{r+1} = (u^{l^*-1}, \mu_{[l^*, r+1]}, \dots, \mu_{[l^*, r+1]}) \quad (29)$$

w.r.t. the vector  $\mu_{[l^*, r+1]} \in \mathbb{R}^C$  of channel-wise means of data  $(g_{l^*}, \dots, g_{r+1})$ . Hence, we obtain a minimizer for full data  $g$  by successively computing  $u^1, u^2, \dots$  until we reach  $u^n$ . An efficient way to evaluate (28) uses precomputed first and second moments of data  $g$  and stores only the jump locations [35]. Thereby, the described method has quadratic worst case time complexity in the data length  $n$  and linear worst case time as well as linear space complexity in the number of channels  $C$  [71]. Additionally, we prune the search space in (28) for speedup as in [71]. Thus, the proposed algorithm can be efficiently applied to vector-valued data with a large number of channels which appear in multi-spectral CT.

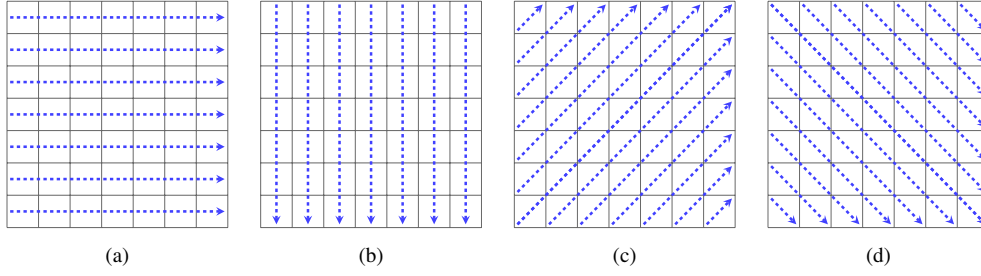


Figure 2: Decomposition of problem (25) into one-dimensional Potts problems along the lines in directions  $d_1, \dots, d_4$  on the discrete image domain  $\Omega$ .

## 5. Potts-Based Superiorization

Superiorization denotes a class of techniques that obtain more regularized results (w.r.t. an appropriately chosen prior) from a basic iterative reconstruction method. SM takes an iterative *basic algorithm* and *perturbs* its iterates employing an exogenous *target function* to obtain a *superior* solution w.r.t. this target function/prior [21]. An example of a basic algorithm that is perturbation resilient is the Landweber iteration for the least squares problem. The Landweber iteration can be superiorized w.r.t. any target function that yields non-ascending directions that are bounded and summable. To fix ideas, if one chooses total variation as the target function [89, 40], such non-ascending directions may be efficiently computed based on directional derivatives. Both energy minimization methods and superiorization methods typically result in two steps within an algorithmic scheme: a forward step followed by a regularizing/perturbation step. However, the interpretation of these steps are different. For such an interpretation and an overview of superiorization and a comparison to (convex) optimization methods, we refer to [21].

We propose methods which take a particular variant of the conjugate gradient method (CG) as the basic algorithm and the (multi-channel) Potts prior (18) as the target function to obtain Potts superiorized, i.e., piecewise constant, solutions. As a result, the iterates are not CG iterates but perturbed versions of them. Thus, the classical result that the CG method converges to a minimizer of the (weighted) least squares problem after a fixed number of iterations cannot be expected to hold anymore. However, we will see that the termination of its perturbed counterpart at an approximate least squares solution may still be ensured.

### 5.1. Perturbing the CG Method with the Block-Wise Potts Prior.

To keep things focused, we first consider single-channel measurements and the simplest anisotropic neighborhood for the Potts prior. In a subsequent section, we provide the extension to multi-channel measurements and the more isotropic neighborhood with diagonal directions.

As a starting point, we consider the penalized weighted least squares model (PWLS) corresponding to the forward operator  $A$ , weights  $W$  and (single-channel) data  $f$ , which is, analogously to (12), given by

$$u^* \in \operatorname{argmin}_u \frac{1}{2} \|Au - f\|_W^2 = \operatorname{argmin}_u \frac{1}{2} \|W^{\frac{1}{2}}Au - W^{\frac{1}{2}}f\|^2. \quad (30)$$

As the next step, we duplicate the objective variable and incorporate the difference between the two variables weighted by a parameter  $\mu > 0$ . This will allow us to apply the CG

method to an overdetermined problem and will serve as the basis for using a block-wise (more accessible) version of the Potts prior. The modified problem is given by

$$(u_1^*, u_2^*) \in \operatorname{argmin}_{u_1, u_2} \frac{1}{2} \left\| \begin{pmatrix} W^{\frac{1}{2}}A & 0 \\ 0 & W^{\frac{1}{2}}A \\ \mu I & -\mu I \end{pmatrix} \begin{pmatrix} u_1 \\ u_2 \end{pmatrix} - \begin{pmatrix} W^{\frac{1}{2}}f \\ W^{\frac{1}{2}}f \\ 0 \end{pmatrix} \right\|^2, \quad (31)$$

where  $I$  denotes the identity. This formulation is inspired by the splitting used in our work [48]. Below we will see that this splitting is necessary since otherwise the Potts perturbation steps would correspond to solving NP-hard problems. Please also note that due to the splitting the least squares system (31) is overdetermined (even when matrix  $A$  is underdetermined) and thus can be solved using the CG method adapted to the least squares problem. The problems (30) and (31) are equivalent in the following sense. A minimizer  $u^*$  of (30) yields via  $(u^*, u^*)$  a minimizer of (31). Conversely, a minimizer  $(u_1^*, u_2^*)$  of (31) satisfies  $u_1^* = u_2^*$  and  $u_1^*$  is a minimizer of (30). We prove this for a more general situation in Proposition 5.5 below. Consequently, we did not alter the original PWLS problem (30).

In contrast to the Landweber method—applying the gradient descent method on the least squares objective—the step sizes of the CG method do not depend on the operator norm of  $A$  which is particularly advantageous for CT problems, where the operator norm of  $A$  is typically large and the Landweber method becomes unfavorable.

In [89], the authors studied several variants of the CG method and identified a particular one which is *strongly perturbation resilient*. That is, its termination is still ensured when its iterates are perturbed by a sequence of (summable) perturbations. In the following, we briefly recall these relations. The pseudocode of a single step of this variant of the CG method is given in Algorithm A.1 in the appendix.

*Strong perturbation resilience.* Strong perturbation resilience is a concept used in the theory of superiorization. It ensures that an iterative algorithm still terminates when its iterates are (appropriately) perturbed. To give a precise definition of strong perturbation resilience, we need some preparations.

As a first step, we denote by  $\mathcal{S}_{\mathcal{T}}$  the solution set of a given problem  $\mathcal{T}$ . Furthermore, we let  $\mathcal{A}$  be an algorithmic operator which generates sequences  $\mathcal{X}_{\mathcal{A}} = (u^k)_{k \in \mathbb{N}_0}$  of the form

$$u^{k+1} = \mathcal{A}(u^k) \quad \text{for all } k \geq 0 \quad (32)$$

that converge to points in  $\mathcal{S}_{\mathcal{T}}$  for any initial  $u^0$ . For our purposes,  $\mathcal{T}$  will correspond to the PWLS (31) and  $\mathcal{S}_{\mathcal{T}}$  to the set of its minimizers.

**Definition 5.1** (Proximity function,  $\varepsilon$ -compatibility, proximity sets). Given a problem  $\mathcal{T}$ , a *proximity function* is a function  $\mathcal{Pr}_{\mathcal{T}}(x) : \mathbb{R}^n \rightarrow [0, \infty)$  that measures how incompatible  $x$  is with  $\mathcal{T}$ . For any  $\varepsilon > 0$  and any proximity function, we define that  $x$  is  $\varepsilon$ -compatible with  $\mathcal{T}$  if  $\mathcal{Pr}_{\mathcal{T}}(x) \leq \varepsilon$ . We call the sets

$$\Gamma_{\varepsilon} = \{x \in \mathbb{R}^n : \mathcal{Pr}_{\mathcal{T}}(x) \leq \varepsilon\} \quad (33)$$

*proximity sets*.

For weighted least squares problems, such as (31), the proximity function is typically given by the residual sum of squares and  $\varepsilon$  is chosen according to the assumed level of noise. Next, we define the notion of an  $\varepsilon$ -output of a sequence w.r.t. a proximity set.

**Algorithm 5.1:** Basic Potts superiorized CG

- 
- 1 Choose an initial perturbation parameter  $\beta_0 > 0$  and an annealing parameter  $0 < a < 1$ , set  $k \leftarrow 0$ . Iterate until stopping criterion:
  - 2 Perform a CG step on  $(u_1, u_2)^k$  w.r.t. the least squares problem (31) and obtain  $(u_1, u_2)^{k+1/2}$ .
  - 3 Perturb the iterate proportionally to  $\beta_k$  with the Potts prior, i.e.,  $(u_1, u_2)^{k+1} \leftarrow \mathcal{P}_{\beta_k}(u_1, u_2)^{k+1/2}$
  - 4 Update  $\beta_{k+1} \leftarrow a\beta_k$ ,  $k \leftarrow k + 1$ . Go to 2.
- 

**Definition 5.2** ( $\varepsilon$ -output of a sequence with respect to  $\Gamma_\varepsilon$ ). For some  $\varepsilon > 0$ , a nonempty proximity set  $\Gamma_\varepsilon$  and a sequence  $\mathcal{X} = (u^k)$  of points, the  $\varepsilon$ -output  $O(\Gamma_\varepsilon, \mathcal{X})$  of  $\mathcal{X}$  w.r.t.  $\Gamma_\varepsilon$  is defined to be the element  $u^k$  with smallest  $k \in \mathbb{N}$  such that  $u^k \in \Gamma_\varepsilon$ .

We can now specify strong perturbation resilience of an algorithmic operator.

**Definition 5.3** (Strong perturbation resilience). Let  $\Gamma_\varepsilon$  denote the proximity set and  $\mathcal{A}$  be an algorithmic operator. The algorithmic scheme (32) is *strongly perturbation resilient* if

- (i) there is an  $\varepsilon > 0$  such that the  $\varepsilon$ -output  $O(\Gamma_\varepsilon, \mathcal{X}_{\mathcal{A}})$  of the sequence  $\mathcal{X}_{\mathcal{A}}$  exists for every initial  $u^0$ ;
- (ii) for all  $\varepsilon \geq 0$  such that  $O(\Gamma_\varepsilon, \mathcal{X}_{\mathcal{A}})$  is defined for every  $u^0$ , we also have that  $O(\Gamma_{\varepsilon'}, \mathcal{Y}_{\mathcal{A}})$  is defined for every  $\varepsilon' \geq \varepsilon$  and for every sequence  $\mathcal{Y}_{\mathcal{A}} = (\bar{u}^k)$  generated by

$$\bar{u}^{k+1} = \mathcal{A}(\bar{u}^k + \beta_k v^k), \quad \text{for all } k \geq 0, \quad (34)$$

where the terms  $\beta_k v^k$  are bounded perturbations, i.e.,  $(v^k)_{k \in \mathbb{N}}$  is bounded,  $\beta_k \geq 0$  for all  $k$  and  $\sum_{k=0}^{\infty} \beta_k < \infty$ .

We record the strong perturbation resilience of the presented variant of the CG method, which has been proven in [89, Theorem A.1].

**Theorem 5.1.** *The CG method as recorded in Algorithm A.1 is strongly perturbation resilient.*

*Perturbations by steps towards the proximal mapping of the block-wise Potts prior.* Towards Potts superiorized solutions, we perturb the iterates of Algorithm A.1 by means of the Potts prior. The basic scheme is summarized in Algorithm 5.1. Typically, in the context of superiorization, the perturbation  $\mathcal{P}_\beta$  in step 3 corresponds to adding a *non-ascending direction* w.r.t. the target function to the current iterate with appropriate step-sizes as in Definition 5.3. Thereby, the target function values of the iterates are decreased so that the final result should become more desirable in terms of the target function. For a smooth target function, a non-ascending direction may be obtained from its negative gradient. Decreasing the parameter  $\beta$  in step 4 ensures that the perturbations –denoted by  $\mathcal{P}_{\beta_k}$  in step 3– become smaller in the course of the iterations and the sequence is summable, i.e.,  $\sum_{k=0}^{\infty} \beta_k < \infty$ .

As the Potts prior is non-smooth, we resort to the evaluation of proximal mappings – a common practice in non-smooth optimization. To this end, we define for  $(u_1, u_2)$  the *block-wise Potts prior*

$$F(u_1, u_2) = \|\nabla_1 u_1\|_0 + \|\nabla_2 u_2\|_0. \quad (35)$$

The block-wise Potts prior (35) counts the number of row-wise jumps in  $u_1$  and the number of column-wise jumps in  $u_2$ . The proximal mapping of  $F$  for  $\beta > 0$  is given by

$$\text{prox}_{\beta F}(u_1, u_2) = \underset{w_1, w_2}{\operatorname{argmin}} F(w_1, w_2) + \frac{1}{2\beta} \|(u_1, u_2) - (w_1, w_2)\|^2. \quad (36)$$



We recall that the right-hand side of (36) is unique for almost all  $u_1, u_2$ , [85], so that using the equality in (36) is reasonable. The proximal mapping (36) can be evaluated efficiently. First, we note that the minimization in (36) can be performed block-wise for  $w_1$  and  $w_2$ , respectively. These smaller problems are instances of (25) for  $\gamma = 2\beta$ , which can be solved by dynamic programming as described in Section 4. Hence, (36) can be efficiently evaluated. In this context, we note that omitting the introduction of  $u_1, u_2$  in (31) would lead to a proximal mapping in a single variable only whose evaluation corresponds to solving a two-dimensional Potts problem which is NP-hard.

It is well-known that the proximal mapping corresponding to a convex lower semicontinuous function can be written in additive form (34) using the generalized gradient [21]. This however, is not feasible for the block-wise Potts prior as it is not convex. Lemma 5.3 will ensure that we still can use (36) to obtain non-ascending directions for the block-wise Potts prior. To this end, we first note the following lemma whose proof can be found in the appendix.

**Lemma 5.2.** *Let  $J_1(w)$  denote the positions of the horizontal jumps of  $w$  and  $J_2(w)$  the positions of vertical jumps of  $w$ , i.e.,  $\{x, x+d_s\} \in J_s(w)$  if and only if  $w(x) \neq w(x+d_s)$ ,  $s = 1, 2$ . Then we have the inclusions  $J_1(\bar{u}_1) \subset J_1(u_1)$  and  $J_2(\bar{u}_2) \subset J_2(u_2)$  for  $(\bar{u}_1, \bar{u}_2) = \text{prox}_{\beta F}(u_1, u_2)$ . In other words, the proximal mapping of the block-wise Potts prior does not introduce jumps which were not already present in its arguments.*

**Lemma 5.3.** *For any  $u = (u_1, u_2)$  and  $\beta \geq 0$ , the vector given by*

$$v = (v_1, v_2) := \begin{cases} \frac{\text{prox}_{\beta F}(u_1, u_2) - (u_1, u_2)}{\delta} & \text{if } \text{prox}_{\beta F}(u_1, u_2) \neq (u_1, u_2), \\ 0 & \text{otherwise,} \end{cases} \quad (37)$$

where  $\delta = \|\text{prox}_{\beta F}(u_1, u_2) - (u_1, u_2)\|$ , satisfies  $\|v\| \leq 1$  and  $F(u + t \cdot v) \leq F(u)$  for all  $t \geq 0$  w.r.t. to the block-wise Potts prior  $F$ . Thus, (37) yields a non-ascending direction for the block-wise Potts prior at  $u = (u_1, u_2)$ .

The proof of Lemma 5.3 can be found in the appendix.

A perturbation strategy for line 3 of Algorithm 5.1 in terms of adding non-ascending directions is now given by

$$\begin{aligned} \mathcal{P}_{\beta_k}((u_1, u_2)^{k+1}) &= \begin{cases} (u_1, u_2)^{k+1/2} + \beta_k \frac{\text{prox}_{\beta_k F}((u_1, u_2)^{k+1/2}) - (u_1, u_2)^{k+1/2}}{\delta} & \text{if } \delta > 0, \\ (u_1, u_2)^{k+1/2} & \text{otherwise} \end{cases} \\ &=: (u_1, u_2)^{k+1/2} + \beta_k \cdot (v_1, v_2)^k, \end{aligned} \quad (38)$$

where  $\delta = \|\text{prox}_{\beta_k F}((u_1, u_2)^{k+1/2}) - (u_1, u_2)^{k+1/2}\|$ . The summability of the parameters  $\beta_k$  by line 4 of Algorithm 5.1 ensures that (38) produces a sequence of bounded perturbations as defined in Definition 5.3. In particular, the sequence  $\beta_k$  of annealing parameters satisfies  $\sum_k \beta_k < \infty$  and the sequence of additive perturbations  $v^k = (v_1, v_2)^k$  is bounded as  $\|v^k\| \leq 1$ .

We summarize the above considerations in the following theorem.

**Theorem 5.4.** *Algorithm 5.1 with the perturbations given by (38), i.e., adding non-ascending directions w.r.t. the block-wise Potts prior, and the stopping criterion*

$$\|W^{\frac{1}{2}}Au_1 - W^{\frac{1}{2}}f\|^2 + \|W^{\frac{1}{2}}Au_2 - W^{\frac{1}{2}}f\|^2 + \|\mu(u_1 - u_2)\|^2 < \varepsilon \quad (39)$$

*terminates for every  $\varepsilon > \varepsilon_0$  and initializations  $u_1, u_2$ , where  $\varepsilon_0$  is the minimal value of the underlying (weighted) least squares problem (30) or, equivalently, (31).*

*Proof.* The proof follows from Theorem 5.1, Lemma 5.3 and property (ii) in Definition 5.3.  $\square$

Concerning the parameters  $\beta_k$ , we used the scaling  $\|A^T f\|_2 / \|A\|_2^2$  to adjust  $\beta_k$  to the scale of the data which corresponds to employing the sequence  $\beta_k = \frac{\|A^T f\|_2}{\|A\|_2^2} \tilde{\beta}_k$ , where  $\tilde{\beta}_k$  is summable, i.e.,  $\sum_k \tilde{\beta}_k < \infty$ , e.g.,  $\tilde{\beta}_k = a^k \beta_0$  for  $0 < a < 1$  and  $\beta_0 > 0$  as in Algorithm 5.1.

*Perturbations by the proximal mapping of the block-wise Potts prior.* We derived perturbations in terms of the block-wise Potts prior by taking a step towards its proximal mapping. By Lemma 5.3 this approach yields a sequence of non-ascending directions w.r.t. the block-wise Potts prior and Theorem 5.4 ensures the termination of the corresponding instance of Algorithm 5.1. As (38) takes a step towards the proximal mapping of the block-wise Potts prior, we may consider perturbations which take the proximal mapping itself, that is,

$$\mathcal{P}_{\beta_k}((u_1, u_2)^{k+1}) = \text{prox}_{\beta_k F}((u_1, u_2)^{k+1/2}). \quad (40)$$

It follows immediately from optimality in the proximal mapping that the block-wise Potts value of  $\mathcal{P}_{\beta_k}((u_1, u_2)^{k+1})$  is lower or equal than the one of  $(u_1, u_2)^{k+1/2}$ . (This also follows from Lemma 5.3.)

In our experiments (see Figure 3), we observed that this perturbation strategy improves upon the perturbations given by (38). Furthermore, the perturbation strategy (40) needs not to be scaled by some constant factor to bring  $(u_1, u_2)^{k+1/2}$  and its perturbation  $\mathcal{P}_{\beta_k}((u_1, u_2)^{k+1})$  to the same scale. We remark that (40) may also be seen as an additive perturbation by defining  $(v_1, v_2)^k = \frac{1}{\beta_k} (\text{prox}_{\beta_k F}((u_1, u_2)^{k+1/2}) - (u_1, u_2)^{k+1/2})$ , so that (40) could be written as  $(u_1, u_2)^{k+1/2} + \beta_k (v_1, v_2)^k$ .

*Remark 5.1.* It is an open question whether (40) yields bounded perturbations in the sense of Definition 5.3. In [21], this was proven for the special case of (smoothed) total variation. The proof uses the Lipschitz continuity of the target function. Unfortunately, neither the Potts prior nor the block-wise Potts prior are even continuous. In general, the results for perturbations obtained from evaluating proximal mappings are rather rare in the literature. However, the practical results encourage future work on this topic.

## 5.2. Potts S-CG

In view of (31), a large choice of  $\mu$  enforces the CG steps to put more emphasis on the deviations between  $u_1$  and  $u_2$ . Thus, large values of  $\mu$  lead to results  $u_1, u_2$  which are closer to each other. Furthermore, the block-wise Potts prior (35) perturbs  $u_1, u_2$  towards row-wise and column-wise piecewise constancy, respectively. In order to obtain solutions which satisfy equality, i.e.,  $u_1 = u_2$ , and which are in addition genuinely piecewise constant, we propose a modified approach of Algorithm 5.1 inspired by penalty methods for energy minimization: after the lines 2-3 in Algorithm 5.1 have been conducted, we increase the coupling parameter  $\mu$ . By starting with a low value  $\mu_0$ , the CG steps give more weight to the data fidelity in the first iterations, while in the later iterations they give more weight to the discrepancies between  $u_1$  and  $u_2$ . Thus, the variables become closer in the later iterations until they become (approximately) equal. This modified superiorization approach which employs perturbations by evaluating proximal mappings is summarized in Algorithm 5.2, which we call *Potts S-CG* (Potts superiorized conjugate gradient).

In Figure 3, we compare the results of the perturbation strategies (38), (40) and the Potts S-CG approach for image reconstruction from undersampled noisy Radon data

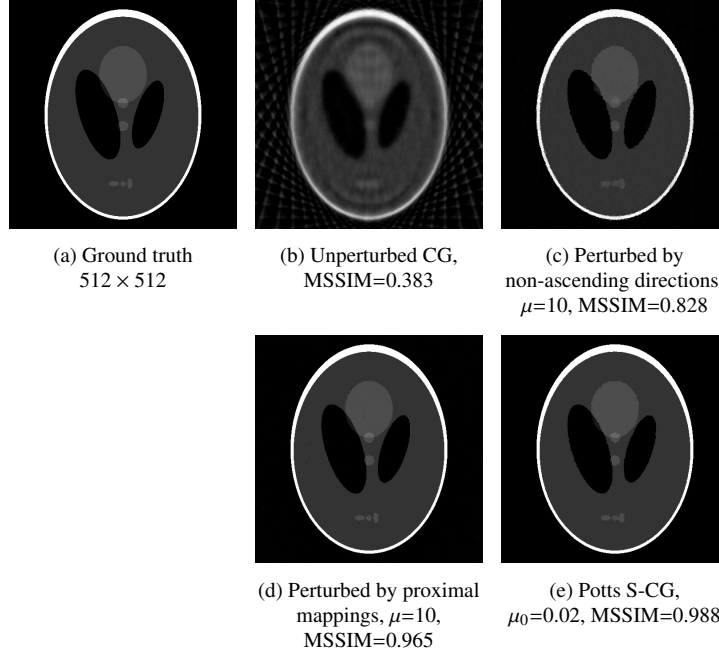


Figure 3: Reconstructions from undersampled Radon data (25 projection angles corrupted by Gaussian noise with  $\sigma = 0.25$ ). (a) Original. (b) Unperturbed CG method. (c) Perturbing the CG iterations with non-ascending directions for the block-wise Potts prior improves upon the unperturbed CG method. (d) Perturbing with the proximal mapping of the block-wise Potts prior yields a further regularized result. (e) The proposed Potts S-CG method produces a less grainy and piecewise constant result and achieves the highest MSSIM value.

---

**Algorithm 5.2:** Basic anisotropic Potts S-CG scheme

---

- 1 Choose an initial perturbation parameter  $\beta_0 > 0$  and coupling parameter  $\mu_0 > 0$ .  
Choose an annealing parameter  $0 < a < 1$ , set  $k \leftarrow 0$ .  
Iterate until  $u_1, u_2$  become equal:
  - 2 Perform a CG step on  $(u_1, u_2)^k$  w.r.t. the least squares problem (31) for  $\mu = \mu_k$  and obtain  $(u_1, u_2)^{k+1/2}$ .
  - 3 Perturb  $(u_1, u_2)^{k+1/2}$  by the proximal mapping of the block-wise Potts prior for the current perturbation parameter  $\beta_k$ , i.e.,  $(u_1, u_2)^{k+1} \leftarrow \text{prox}_{\beta_k F}(u_1, u_2)^{k+1/2}$ .
  - 4 Update  $\beta_{k+1} \leftarrow a\beta_k$ , increase the coupling parameter  $\mu_{k+1} \leftarrow (\mu_0\beta_0)/\beta_k$ ,  $k \leftarrow k + 1$ .
  - 5 Go to 2.
- 

(measurements from 25 projection angles corrupted by Gaussian noise of variance  $\sigma = 0.25$ ). Please note that this corresponds to a simplified model compared to the more accurate model (10). However, we use this simplified model to obtain an initial comparison of the presented Potts superiorization methods. For the perturbation strategies (38), (40), we used the coupling parameter  $\mu = 10$  and the stopping rule (39) with  $\varepsilon = m\sigma^2 + \mu^2$ , where  $m$  denotes the total number of measurements. Potts S-CG used the initial coupling parameter  $\mu_0 = 0.02$  and the iteration was stopped when  $u_1, u_2$  became (approximately) equal. All three approaches used the annealing parameters  $a = 0.99$  and  $\beta_0 = 1$ . We observe that all perturbation strategies

improve upon unperturbed CG. Furthermore, we see that taking the proximal mapping (40) produces a more regularized solution than adding non-ascending directions (38). Finally, the result of Potts S-CG is genuinely piecewise constant and has the highest mean structural similarity index (MSSIM). (We refer to Section 7 for more details on the MSSIM.)

In the following, we give further details on the Potts S-CG approach. In particular, we describe the extensions to more isotropic solutions and multi-channel data.

*Extension to more isotropic discretizations and multi-channel measurements.* We extend the Potts S-CG approach to more isotropic discretizations, i.e., directions  $d_1, \dots, d_S$ , and multi-channel measurements  $f$ . First, we note that the basic PWLS problem for multi-channel measurements is given by the channel-wise sum

$$\min_u \sum_{c=1}^C \frac{1}{2} \|W_c^{\frac{1}{2}} A u_c - W_c^{\frac{1}{2}} f_c\|^2. \quad (41)$$

As a preparation, we define the block-matrices  $\bar{A}_{\mu,c}$  given by

$$\bar{A}_{\mu,c} = \begin{pmatrix} W_c^{\frac{1}{2}} A & & & & & \\ & W_c^{\frac{1}{2}} A & & & & \\ & & \ddots & & & \\ & & & W_c^{\frac{1}{2}} A & & \\ \mu I & -\mu I & 0 & \dots & 0 & 0 \\ \mu I & 0 & -\mu I & \dots & 0 & 0 \\ & \vdots & & & \vdots & \\ \mu I & 0 & 0 & \dots & -\mu I & \\ 0 & \mu I & -\mu I & \dots & 0 & 0 \\ & \vdots & & & \vdots & \\ 0 & \mu I & 0 & \dots & 0 & -\mu I \\ & \vdots & & & \vdots & \\ 0 & 0 & 0 & \dots & \mu I & -\mu I \end{pmatrix} \quad \text{and} \quad \bar{f}_c = \begin{pmatrix} W_c^{\frac{1}{2}} f_c \\ W_c^{\frac{1}{2}} f_c \\ \vdots \\ W_c^{\frac{1}{2}} f_c \\ 0 \\ 0 \\ \vdots \\ \vdots \\ \vdots \\ \vdots \\ \vdots \\ \vdots \\ 0 \end{pmatrix}. \quad (42)$$

The upper block part of  $\bar{A}_{\mu,c}$  realizes the data fidelities for the  $c$ -th channel and its lower part the mutual deviations between the variables  $(u_1, \dots, u_S)$  in the  $c$ -th channel. Please note that we use the notation  $u_{s,c}$  to refer to the  $c$ -th channel of  $u_s$ . Using this notation we can now formulate the corresponding PWLS problem, that is, the counterpart of (31); it is given by

$$(u_1^*, \dots, u_S^*) \in \operatorname{argmin}_{u_1, \dots, u_S} \sum_{c=1}^C \frac{1}{2} \|\bar{A}_{\mu,c} (u_{1,c}, \dots, u_{S,c})^T - \bar{f}_c\|^2 \quad (43)$$

and the corresponding normal equations for each channel are given by

$$\bar{A}_{\mu,c}^T \bar{A}_{\mu,c} (u_{1,c}, \dots, u_{S,c})^T = \bar{A}_{\mu,c}^T \bar{f}_c. \quad (44)$$

After evaluating the multiplications in (44), we obtain the following more explicit equations

$$\begin{pmatrix} \sum_{t=2}^S \mu^2(u_{1,c} - u_{t,c}) + A^T W_c A u_{1,c} \\ \vdots \\ \sum_{t \neq s}^S \mu^2(u_{s,c} - u_{t,c}) + A^T W_c A u_{s,c} \\ \vdots \\ \sum_{t=1}^{S-1} \mu^2(u_{S,c} - u_{t,c}) + A^T W_c A u_{S,c} \end{pmatrix} = \begin{pmatrix} A^T W_c f_c \\ \vdots \\ A^T W_c f_c \\ \vdots \\ A^T W_c f_c \end{pmatrix} \quad (45)$$

for each channel  $c = 1, \dots, C$ . The next proposition establishes the relation between the basic weighted least squares problem (41) and its augmented counterpart (43). A proof can be found in the appendix.

**Proposition 5.5.** (i) A minimizer  $u^*$  of the least squares problem (41) induces a minimizer of the augmented least squares problem (43) via  $(u^*, \dots, u^*)$ . (ii) A minimizer  $(u_1^*, \dots, u_S^*)$  of the augmented least squares problem (43) satisfies  $u_1^* = \dots = u_S^*$ . Further,  $u_1^*$  is a minimizer of (41) as well. (iii) If  $A$  has full column rank, then  $u^*$  is the (unique) minimizer of (41) if and only if  $(u^*, \dots, u^*)$  is the (unique) minimizer of (43).

By following the lines of the general CG algorithm (cf. Algorithm A.1 in the appendix), the CG step specifically for (45) is given by Algorithm A.2 in the appendix.

Next, we derive the perturbation step by means of the proximal mapping of the block-wise Potts prior with  $S$  directions. We defined the block-wise Potts prior for the special case  $S = 2$  in (35). For the more general situation with  $S$  directions as above, it is given by

$$F(u_1, \dots, u_S) = \sum_{s=1}^S \omega_s \|\nabla_{d_s} u_s\|_0. \quad (46)$$

(Recall the definition of  $\|\nabla_{d_s} u_s\|_0$  in (17) and the weights  $\omega_s$  from Section 3.1.) To perturb the CG iterates of (45) by means of the block-wise Potts prior (46), we need to evaluate its proximal mapping as above. The proximal mapping of the block-wise Potts prior for  $S$  directions (46) is defined by

$$\text{prox}_{\beta F}(u_1, \dots, u_S) = \underset{w_1, \dots, w_S}{\text{argmin}} F(w_1, \dots, w_S) + \frac{1}{2\beta} \sum_{s=1}^S \|u_s - w_s\|^2. \quad (47)$$

As seen in Section 4, the minimization in (47) decomposes into problems, which depend on one of the  $u_s$  only. These smaller problems are of the form (25), which can be efficiently solved by dynamic programming as described in Section 4. We provide the pseudocode of the Potts S-CG for more isotropic discretizations and multi-channel data in Algorithm 5.3.

## 6. Comparison of Potts ADMM and Potts S-CG

*Handling the forward operator.* Potts ADMM introduces an additional splitting variable  $v$  in (19) to cope with the forward operator  $A$ . Consequently, one has to solve a  $\ell_2$ -regularized problem (21) w.r.t.  $A$  and  $v$  in each iteration of Potts ADMM. In contrast, Potts S-CG does not introduce such a splitting variable and only requires a CG step w.r.t.  $A$  in each iteration, i.e., it requires only applying  $A$  and  $A^T$  in each iteration instead of solving a  $\ell_2$ -regularized problem. As a result, Potts S-CG needs more iterations, while the iterations are cheaper than in Potts ADMM (Figure 4: Potts S-CG 0.95 sec/iteration, Potts ADMM 2.35 sec/iteration).

**Algorithm 5.3:** Potts S-CG

---

**Input:** Forward operator  $A \in \mathbb{R}^{m \times n^2}$ , multispectral sinogram  $f \in \mathbb{R}^{m \times c}$ , PWLS weights  $W \in \mathbb{R}^{m \times m}$ , annealing parameter  $0 < a < 1$ , initial parameters  $\beta_0, \mu_0 > 0$ , stopping parameter  $\text{tol} > 0$

**Output:**  $u^* \in \mathbb{R}^{n \times n \times C}$

---

```

1 Initialize for all  $s = 1, \dots, S$ :
2  $u_s^0 = A^T W f$ ,  $p_s^0 = A^T W f$ ,  $h_s^0 = A^T W A p_s^0 + \sum_{t \neq s} \mu_0^2 (p_s^0 - p_t^0)$ 
3  $k = 0$ 
4 repeat
    /* Increase the splitting penalty parameter proportionally to  $\beta_k$  */
5      $\mu_k \leftarrow (\mu_0 \beta_0) / \beta_k$ 
    /* Perturb the iterates with the block-wise Potts prior by solving line-wise Potts problems for jump
       penalty  $2\beta_k$ : */
6      $(u_1, \dots, u_S)^{k+1/2} = \operatorname{argmin}_{w_1, \dots, w_S} \sum_s \|u_s^k - w_s\|^2 + 2\beta_k \omega_s \|\nabla_{d_s} w_s\|_0$ 
    /* Perform a CG step on  $(u_1, \dots, u_S)^{k+1/2}$  w.r.t. the weighted normal equations (45): */
7     for  $c = 1, \dots, C$  do
8         Compute  $u_{s,c}^{k+1}, h_{s,c}^{k+1}, p_{s,c}^{k+1}$  from  $u_{s,c}^{k+1/2}, h_{s,c}^k, p_{s,c}^k$  for all  $s = 1, \dots, S$  by
            Algorithm A.2 for  $\mu = \mu_k$ 
9     end
10     $\beta_{k+1} \leftarrow a\beta_k$ 
11     $k \leftarrow k + 1$ 
12 until  $\|u_s^k - u_{s+1}^k\|_\infty < \text{tol}$  for all  $s = 1, \dots, S - 1$ ;
13 return  $u^* = \frac{1}{S} \sum_{s=1}^S u_s^k$ 

```

---

*Comparison for multi-channel Radon data.* Next, we consider the reconstruction of a colored, i.e., three-channel, Shepp-Logan Phantom from undersampled multi-channel Radon data corrupted by additive Gaussian noise (20 angles,  $\sigma = 0.35$ ). Further, we study the data deviation,  $\frac{1}{S} \sum_{s,c} \|A u_{s,c}^k - f_c\|^2$ , and the block-wise Potts prior,  $\sum_s \omega_s \|\nabla_{d_s} u_s^k\|_0$ , as a function of the iteration index. To put the results into context, we also include the reconstruction result and iteration data of a penalty method for the Potts model which relaxes the constrained problem (19) by replacing the constraints by a sequence of softened constraints. To fix ideas, this method corresponds to Potts ADMM with the Lagrange multipliers set to zero. Furthermore, we include the Potts superiorized Landweber method (Potts S-Landweber), which corresponds to Potts S-CG with Landweber steps instead of CG steps. Recall that a Landweber step corresponds to a gradient descent step w.r.t. the (weighted) least squares problem (41).

In Figure 4, we show the results. First, we note that the jumps of all results are spatially aligned across the channels which illustrates the considerations on the multi-channel Potts prior in Section 3.2. Concerning the reconstruction quality, we observe that the penalty method as well as Potts S-Landweber produce spurious artifacts near segment boundaries. Potts ADMM and Potts S-CG yield improved reconstruction results which are close to the ground truth. This confirms the theoretical consideration of Section 5.1 that the Landweber method is not a favorable basic algorithm in the sense of superiorization, when large operator norms are involved. Moreover, the results confirm that the Lagrange multipliers in Potts ADMM (the “memory” of the iterations) play a crucial role for the reconstruction quality.

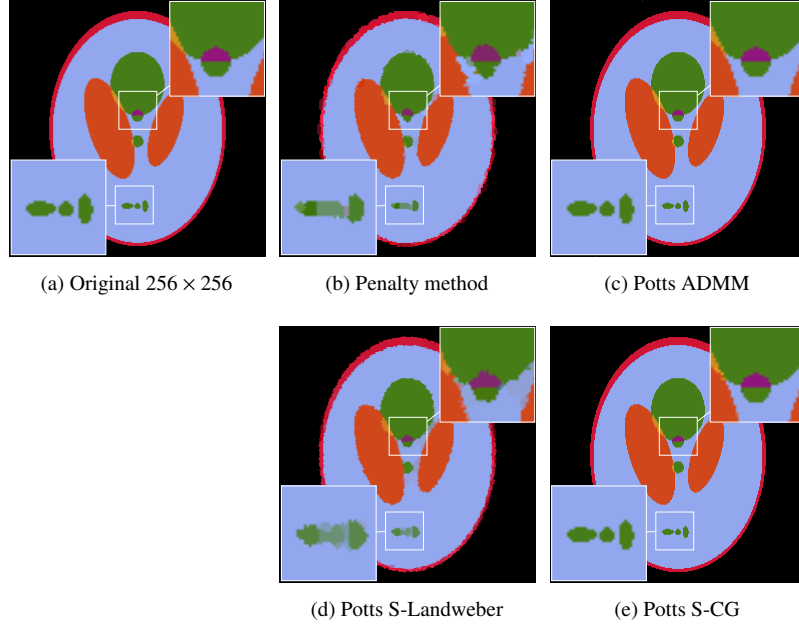


Figure 4: Potts ADMM and Potts S-CG for undersampled noisy multi-channel Radon data (20 angles,  $\sigma = 0.35$ ). The jumps of all results are spatially aligned across the channels. However, the penalty method and Potts S-Landweber produce some spurious artifacts near the segment boundaries which can be seen particularly in the zoomed regions. Potts ADMM and Potts S-CG produce improved reconstruction results which are close to the ground truth. On close inspection, we observe that some of the segment boundaries are briefly smoother in the Potts ADMM result than in the Potts S-CG result (see, e.g., the zoomed regions).

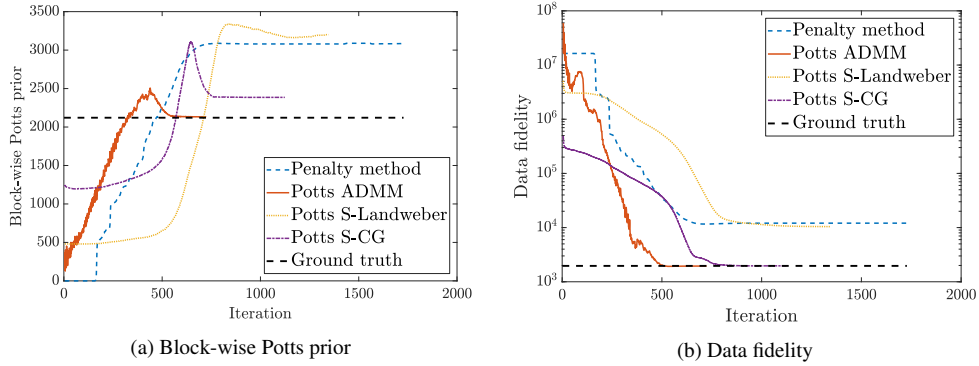


Figure 5: Values of the block-wise Potts prior (46) and the data deviations over the iterations for the results in Figure 4. Potts ADMM and Potts S-CG achieve block-wise Potts prior values and data deviations which are near the respective values of the ground truth. This reflects the qualitative findings in Figure 4 as it shows that the solutions of Potts ADMM and Potts S-CG simultaneously agree with the data and minimize the (block-wise) Potts prior.

These qualitative findings are reflected by the graphs in Figure 5 which show the values of the block-wise Potts prior (46) and the data deviations over the iterations: Potts ADMM and Potts



Method	Initialization	Stopping criterion
FISTA TV	0	number of iterations: $k = \text{maxIter}$
FISTA TNV	0	number of iterations: $k = \text{maxIter}$
FISTA dTVp	0	number of iterations: $k = \text{maxIter}$
Potts ADMM	0	distance of variables: $\ u_s^k - u_{s+1}^k\ _\infty < \text{tol}$
Potts S-CG	$A^T W f$	distance of variables: $\ u_s^k - u_{s+1}^k\ _\infty < \text{tol}$

Table 1: List of initializations and stopping criteria of the considered methods. In our experiments, we used the parameters  $\text{maxIter} = 250$ , see [46], and  $\text{tol} = 10^{-5}$ . The methods are quantitatively compared in terms of the achieved mean structural similarity index (MSSIM) (54).

S-CG arrive at values which are close to the values of the ground truth. This illustrates that the results of Potts ADMM and Potts S-CG agree with the data and at the same time minimize the (block-wise) Potts prior.

## 7. Experimental Results

In this section, we illustrate the potential of the Potts prior for multi-spectral computed tomography. More precisely, we consider the Potts S-CG algorithm (Algorithm 5.3) and the Potts ADMM algorithm (Algorithm 4.1) and compare them with existing TV-type approaches. First, we provide the necessary implementation details of Potts ADMM and Potts S-CG. Next, we briefly recall the TV, TNV and dTVp prior. To obtain a qualitative comparison, we consider the geocore phantom used in [46]. Finally, we give a quantitative comparison of the methods for a phantom which consists of few organic materials.

*Implementation details.* We provide the necessary implementation details. We begin with Potts ADMM (Algorithm 4.1). As coupling sequences, we employ  $\rho_k = 10^{-7} \cdot k^{2.01}$ ,  $\mu_k = \rho_k/S$ . For the stopping criterion, we set  $\text{tol} = 10^{-5}$ . We solve the subproblems (21) using Matlab’s built-in function `pcg` which is applied to the weighted normal equations (24) with standard tolerance  $10^{-6}$  and a maximum number of 2000 iterations. We use the previous iteration  $v^{k-1}$  as initial guess so that after the first ADMM iterations only a few `pcg` iterations are needed. Regarding Potts S-CG (Algorithm 5.3), we used the annealing parameter  $a = 0.999$  and the initial coupling  $\mu_0 = 10^{-4}$ . For the stopping criterion, we set  $\text{tol} = 10^{-5}$ . The ADMM subproblems (22) in Potts ADMM and the evaluation of the proximal mappings (47) in Potts S-CG are solved by using the Potts solver provided by the Pottslab software toolbox which makes use of parallelization for multicore CPUs (<https://github.com/mstorath/Pottslab>). For 3D-data and large problem sizes an implementation using the GPU becomes reasonable. However, such an implementation is beyond the scope of this paper.

*Methods for comparison.* We compare the Potts ADMM and the Potts S-CG method with classical channel-wise total variation (TV), channel-coupling total nuclear variation (TNV) [62] and the probabilistic directional TV method (dTVp), which was proposed in [46]. Channel-wise TV corresponds to the  $\ell_1$ -norm of the discrete gradient  $\|\nabla u\|_1$  for each channel

separately. Its application amounts to solving the convex problem given by

$$\operatorname{argmin}_u \sum_{c=1}^C \|Au_c - f_c\|_W + \alpha \|\nabla u_c\|_1 \quad (48)$$

for a parameter  $\alpha > 0$ . The TNV regularizer uses the nuclear norm of the discrete Jacobian in each pixel of a multi-channel image to correlate the channels. Applying TNV corresponds to the convex problem

$$\operatorname{argmin}_u \sum_{c=1}^C \|Au_c - f_c\|_W + \sum_{x \in \Omega} \alpha \|Du(x)\|_*, \quad (49)$$

where  $\alpha > 0$  is a parameter,  $Du(x)$  is the  $2 \times C$  matrix of channel-wise finite differences of  $u$  at the point  $x$  and  $\|\cdot\|_*$  denotes its nuclear norm, i.e., the sum of its singular vales. The dTVp regularizer is a modification of the directional TV (dTV) regularizer. The dTV regularizer enforces correlation between a channel image  $w$  and a reference channel  $v$  by means of the directional diffusion of the channel given the known reference channel. To fix ideas, we denote by  $\operatorname{vec}(w) \in \mathbb{R}^{n^2}$  the column-wise vectorization of  $w$  and by  $D_x$  the  $2 \times n^2$ -matrix such that  $D_x \operatorname{vec}(w)$  is the finite differences vector of  $w$  at the point  $x$ . Then, the dTV regularizer is given by

$$\operatorname{dTV}(w, v) = \sum_{x \in \Omega'} \|P_v D_x \operatorname{vec}(w)\|_2, \quad P_v = \begin{cases} I - \frac{D_x \operatorname{vec}(v) \operatorname{vec}(v)^T D_x^T}{\|D_x \operatorname{vec}(v)\|^2} & \text{if } D_x \operatorname{vec}(v) \neq 0, \\ I & \text{if } D_x \operatorname{vec}(v) = 0 \end{cases} \quad (50)$$

for a single-channel image  $w$  and reference  $v$ . The multi-channel version of (50) is given by

$$\sum_{c=1}^C \operatorname{dTV}(u_c, v_c), \quad (51)$$

where  $v_c$  denote the reference channel for  $u_c$ . In contrast to dTV, for dTVp the reference channels are not fixed, but chosen probabilistically in each iteration of the reconstruction process. The reference channels are chosen among the channels of the former iterate of  $u$ . This process uses a probability mass function, which is based on the channel-wise geometric mean of the estimated signal-to-noise ratios (SNR). Hence, channels with high SNR are more likely to become a reference channel. We note that the dTVp regularizer is non-convex [46].

We used the implementation of [46], which employs the FISTA method (fast iterative shrinkage-thresholding) [7] to approach the respective minimization problems (<https://github.com/dkazanc/multi-channel-x-ray-CT>). The FISTA method converges to the global minimizer for the convex regularizers TV and TNV. However, this does not necessarily hold for dTVp which is non-convex. In Table 1, we list the considered methods together with their respective initializations and stopping criteria.

*Assessment of the reconstruction quality.* We discuss quality measures for reconstructions of compound bodies. A standard choice corresponds to the root mean square error (RMSE). For  $u, v \in \mathbb{R}^{n \times n}$  it is given by

$$\operatorname{RMSE}(u, v) = \sqrt{\frac{1}{n^2} \sum_{j=1}^{n^2} |u(j) - v(j)|^2} \cdot 100, \quad (52)$$

where we use the factor 100 for scaling. However, it is well-known that error measures based on the  $\ell_2$ -distance such as the RMSE are sensitive to outliers which may only mildly affect the

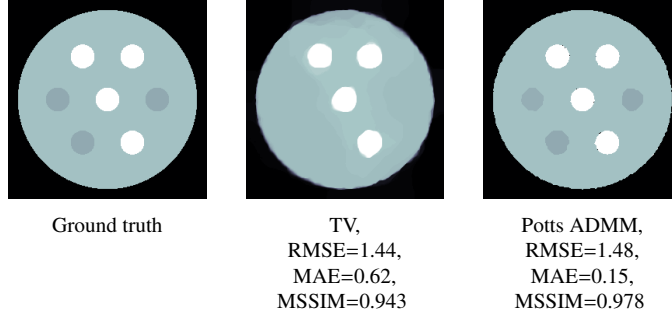


Figure 6: Comparison of error measures for the reconstruction of a compound body (excerpt from Figure 12). Even though TV smooths out some of the spheres, it achieves lower RMSE than Potts ADMM which preserves these spheres. The larger RMSE of Potts ADMM may be attributed to few outliers at the boundaries of the white spheres. In comparison, Potts ADMM achieves lower MAE and higher, i.e., more preferable, MSSIM than TV. This illustrates the sensitivity of RMSE to outliers in the reconstruction.

reconstruction quality. Outliers consisting of only few pixels can often be removed by a basic post-processing, e.g. median filtering. An alternative distance that is less sensitive to outliers corresponds to the mean absolute error (MAE) which is given by

$$\text{MAE}(u, v) = \frac{1}{n^2} \sum_{j=1}^{n^2} |u(j) - v(j)| \cdot 100, \quad (53)$$

where the factor 100 is again used for scaling. A quality measure which was developed to reflect the visual similarity between images better than classical pointwise measures is the mean structural similarity index (MSSIM) [81]. It is given by

$$\text{MSSIM}(u, v) = \frac{1}{n^2} \sum_{x \in \Omega'} \frac{(2\mu_u \mu_v + C_1)(2\sigma_{uv} + C_2)}{(\mu_u^2 + \mu_v^2 + C_1)(\sigma_u^2 + \sigma_v^2 + C_2)} \quad (54)$$

for the mean intensity  $\mu$  and standard deviation  $\sigma$  of a  $11 \times 11$ -window centered at pixel  $x$  weighted by a circular-symmetric Gaussian weighting function with standard deviation 1.5 normalized to unit sum. The constants are set to  $C_1 = 10^{-4}$ ,  $C_2 = 9 \cdot 10^{-4}$ . The MSSIM is bounded from above by 1 and higher values are preferable. We use the Matlab implementation of the MSSIM. Please note that for comparing piecewise constant images, the Rand index would be a suitable quality measure as well since it quantifies directly the similarity between clusters/segmentations [61, 2]. However, as TV-based priors typically yield results which are not piecewise constant, we refrain from using the Rand index.

In Figure 6, we compare RMSE, MAE and MSSIM for the reconstruction of a piecewise constant image with TV and Potts ADMM. We note that TV smoothed out whole regions of the ground truth, while Potts ADMM reconstructs these regions and distinguishes them sharply from the surrounding region. Nevertheless TV achieves a lower RMSE than Potts ADMM. On the other hand, Potts ADMM achieves lower MAE and higher MSSIM, respectively, than TV as MAE and MSSIM are less sensitive to outliers. We attribute the higher RMSE of Potts ADMM to only few outliers at the boundaries of some of the white segments. Thus, the MSSIM seems to be more suitable than RMSE for comparing reconstruction qualities in the present setup. However, we report the MSSIM, MAE and RMSE in our experiments.

*Geocore phantom.* We start out with a qualitative comparison w.r.t. the geocore phantom of [46]. The phantom has size  $512 \times 512$  and consists of four materials: quartz, pyrite, galena, and gold; see Figure 7. The width of the domain is set 1 cm, the distance from the X-ray source to the rotation center to 3 cm, the distance from the source to the detector is 5 cm and the width of the detector array is 2 cm. The X-ray spectrum was simulated with the spektr software package [68]. The energy spectrum of the emitted photons is shown in Figure 8 for the used tube potential (120 kVp) and photon flux  $I_0 = 4 \cdot 10^4$ . The photon attenuation coefficients for the materials were obtained from the PhotonAttenuation software package [75]. The energy range is chosen as 45-114 keV and is discretized into 70 energy bins. The multi-spectral measurements were simulated with the Astra-Toolbox [76]. In particular, we set the fan-beam scanning geometry and obtained the measurements according to 120 projection angles from a larger version of the phantom ( $1024 \times 1024$ ). For TV, TNV and dTVp, we used the model parameters as given in [46], i.e.,  $\alpha_{TV} = 4.2 \cdot 10^{-4}$ ,  $\alpha_{TNV} = 1.2 \cdot 10^{-3}$  and  $\alpha_{dTVp} = 3.3 \cdot 10^{-3}$ . Potts ADMM used the jump penalty  $\gamma = 0.075$  and Potts S-CG the initial perturbation parameter  $\beta_0 = 500$ .

In Figure 9, we show the reconstructions for three depicted channels. We observe that Potts ADMM and Potts S-CG produce sharp boundaries across the channels, while also showing considerably fewer artifacts than the methods of comparison. These qualitative findings are confirmed by the corresponding MSSIM values (see also Figure 8) which are higher for Potts ADMM and Potts S-CG for the majority of the channels.

*Organic spheres phantom.* In the last paragraph, we considered the geocore phantom, which consisted of inorganic materials, many energy channels and a moderate number of projections were available. Next, we conduct a quantitative comparison in terms of a phantom, which consists of organic materials and only few energy bins and projection angles are available. To this end, we consider the  $256 \times 256$  phantom of Figure 10, which consists of homogeneous regions filled with muscle, fat and bone tissue. The domain and detector width as well as the distances involved in the measurement process are the same as for the geocore phantom. The X-ray spectrum as well as the LAC's of muscle, fat and bone were simulated with the spektr software package for the used tube potential (150 kVp) and photon flux  $I_0 = 10^5$ . In this context, we note that the measurements were simulated according to (6) to avoid the inverse crime. Then, for the reconstruction, the linear model (7) was used. We show the LAC's of the involved materials and the X-ray spectrum in Figure 11. The detectors bin the X-ray spectrum into three energy bins. We note that the LAC's of fat and muscle tissue are very close, especially for higher energies. Thus, the reconstruction approaches should aid the recovery of the third channel (the one which holds highest energies among the three channels) by employing the other two (less problematic) channels. Again, we simulate the measurements with the Astra-toolbox and use a fan-beam scanning geometry with 25 projection angles (obtained from a larger  $512 \times 512$  version of the phantom). Hence, the reconstruction approaches have to deal with the additional challenge of highly undersampled measurements.

The individual model parameters were chosen empirically. More precisely, we determined the model parameters by choosing the optimal ones w.r.t. to the mean value of the channel-wise MSSIM's. In particular, for TV and TNV, the optimal parameter  $\alpha$  was chosen among  $\{10^{-4}, 1.5 \cdot 10^{-4}, \dots, 10^{-3}\}$ . As dTVp is of probabilistic nature, we repeated the computation for each parameter  $\alpha$  five times and chose the best result. Here, we let  $\alpha \in \{10^{-4}, 2 \cdot 10^{-4}, \dots, 2 \cdot 10^{-3}\}$ . The jump penalty of Potts ADMM was chosen from  $\gamma \in \{10^{-5}, 2 \cdot 10^{-5}, \dots, 2 \cdot 10^{-4}\}$  and for Potts S-CG, the initial perturbation parameter was obtained from  $\beta_0 \in \{1, \dots, 20\}$ .

In Figure 12, we show the reconstructions together with the corresponding (optimal)

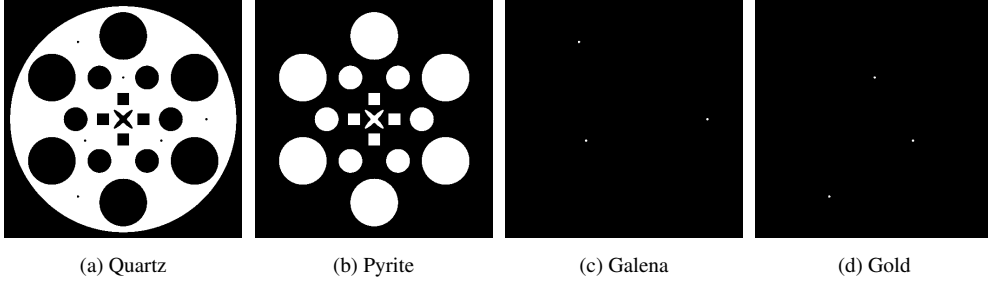


Figure 7: The geocore phantom consists of four inorganic materials: (a) quartz, (b) pyrite, (c) galena and (d) gold. The background is air.

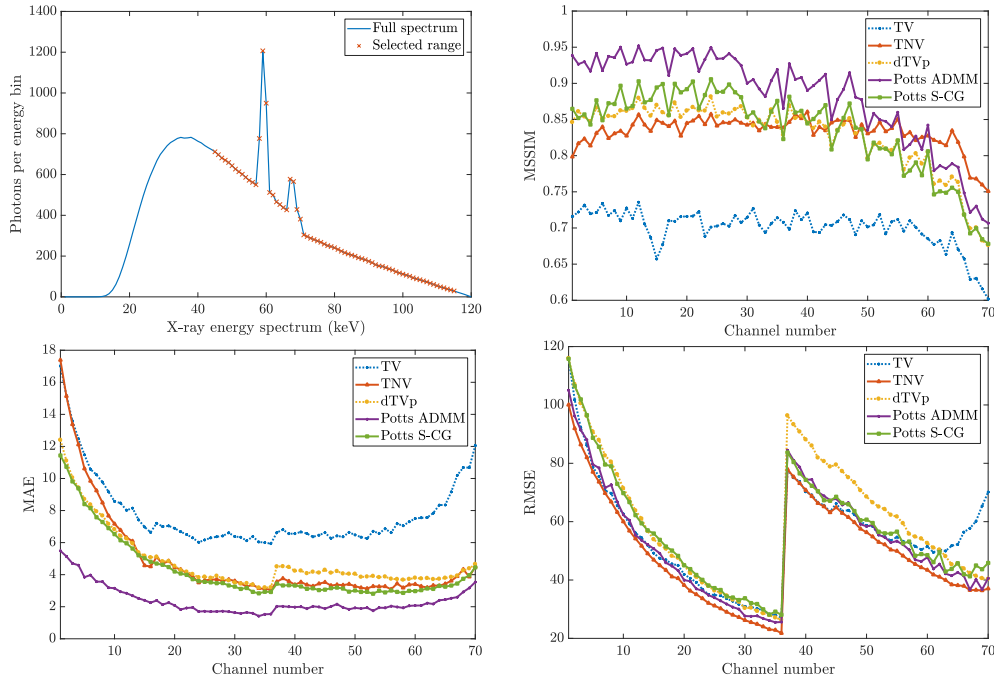


Figure 8: *Top left*: The full X-ray spectrum and the range of energies (45-114 keV) used for modeling the measurements of the geocore phantom. The spectrum is discretized into 70 energy bins. *Top right*: MSSIM of the reconstructions of the geocore phantom for all energy bins. The channel-coupling methods have larger MSSIM values than channel-wise TV. For the majority of the energies the result of Potts ADMM and Potts S-CG have higher MSSIM values than the TV-type regularizers dTVp and TNV (Potts ADMM: 57 channels, Potts S-CG: 38 channels). *Bottom*: MAE and RMSE of the reconstructions of the geocore phantom. For the highest energies, which are particularly prone to noise, the channel-coupling methods have considerably lower MAE and RMSE than channel-wise TV. Potts ADMM and Potts S-CG achieve the lowest MAE for most of the energies, while the RMSE of the methods are close for most energies. (The jump in the RMSE at the 36th channel may be attributed to a sudden increase of the LAC of gold at roughly 80 keV.)

MSSIM. We observe that Potts ADMM and Potts S-CG achieve the highest MSSIM values for all three channels and the MSSIM values of Potts ADMM and Potts S-CG are rather close.

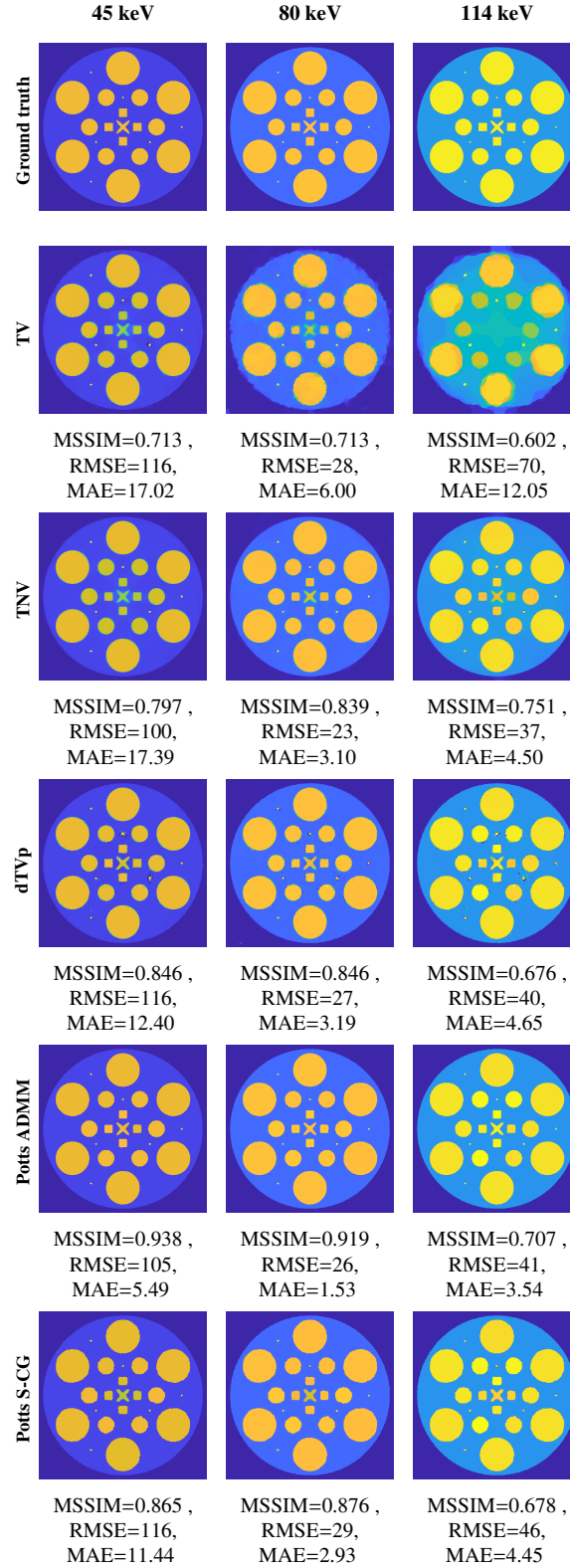


Figure 9: Reconstruction results of the geocore phantom for three selected energy bins. Channel-wise TV exhibits artifacts at the segment boundaries in the second channel and does not recover the inner segments in the third channel. TNV yields an improved reconstruction, but still shows (blueish) artifacts at the segment boundaries. The dTVp result has sharper boundaries than TV and TNV, but the artifacts at the segment boundaries are still present. The Potts ADMM and the Potts S-CG results show less artifacts and the boundaries are sharp. Further, they achieve the highest MSSIM values for two out of the three depicted channels, which is representative for the full energy spectrum; see Figure 8.

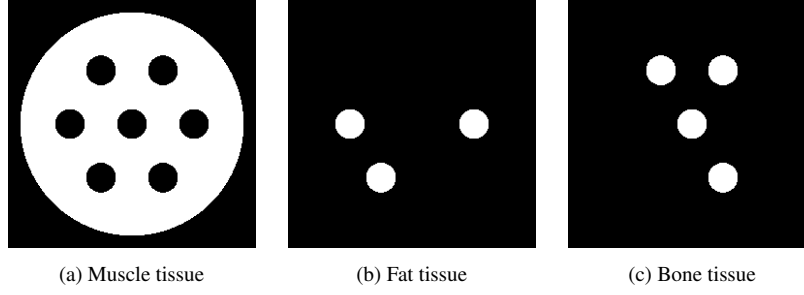


Figure 10: The organic spheres phantom consists of three materials. (a) Muscle tissue, (b) fat tissue and (c) bone tissue. The background is air. The main challenge is to separate the regions with muscle tissue and those with fat tissue as fat and muscle have very similar LAC's throughout the considered energy spectrum; see Figure 11.

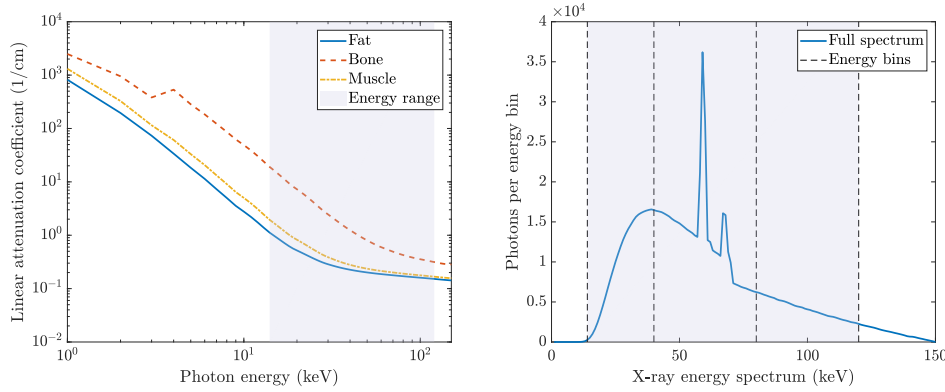


Figure 11: Modeling the measurements of the organic spheres phantom. *Left*: the LAC's of fat, bone and muscle tissue. The highlighted area depicts the used energy range. The LAC curves of fat and muscle are close. *Right*: the full X-ray spectrum and the used energy range (15-120 keV) for modeling the data of the organic spheres phantom. The spectrum is binned into three energy bins by the detectors and their boundaries are depicted by the dashed vertical lines.

Furthermore, the fact that Potts ADMM and Potts S-CG achieve higher MSSIM values than the other methods is reflected by the reconstructions: the result of channel-wise TV exhibits blurry boundaries and the segments corresponding to the fat tissue are not recovered in the third channel. TNV provides an improved reconstruction of the third channel. However, the segment boundaries remain diffuse. The dTVp method produces sharp boundaries in all three channels, but introduces some spurious artifacts near the boundaries. Potts ADMM and Potts S-CG recover the segments and provide sharp boundaries throughout the channels. Further, they show fewer artifacts.

## 8. Conclusion

We considered the reconstruction problem in multi-spectral CT, focusing on indirect measurements from energy-discriminating photon-counting detectors. We proposed the



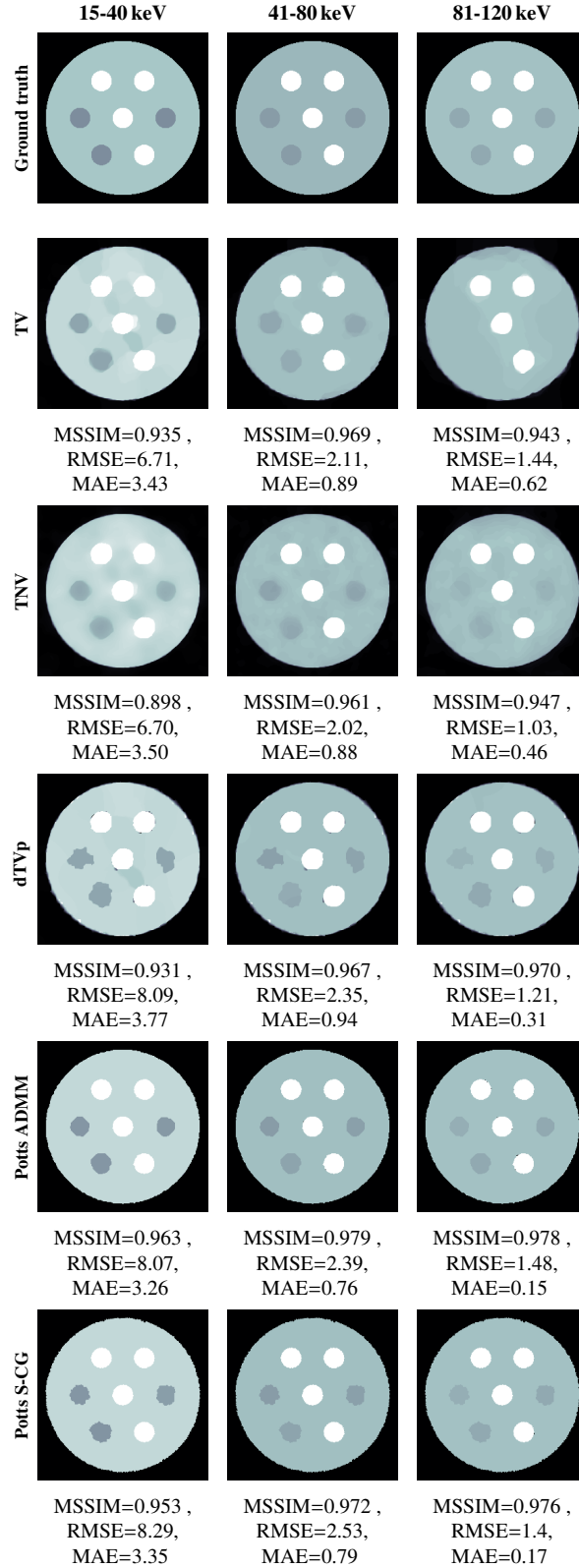


Figure 12: Reconstruction of the organic spheres phantom. The channel-wise TV result exhibit blurry boundaries and smooths out the fat segments in the third channel. TNV yields an improved reconstruction for the third channel. However, the boundaries are still blurry. The dTVp method produces sharp boundaries in all three channels, but introduces some spurious artifacts near the boundaries. Potts ADMM and Potts S-CG recover the segments and provide sharp boundaries throughout the channels. Further, they show fewer artifacts and achieve the highest MSSIM values for all three channels.

multi-channel Potts prior which promotes piecewise constant reconstructions. We found that the multi-channel Potts prior provides a strong channel coupling in that the jumps in the solution are enforced to be at the same spatial positions across the channels. This property is especially beneficial for multi-channel images in multi-spectral CT as their channels have a strong structural correlation. We employ the multi-channel Potts prior by minimizing the multi-channel Potts model. To this end, we adapted the ADMM strategy proposed in [73] to the multi-channel reconstruction problem in multi-spectral CT. Furthermore, we proposed new reconstruction approaches based on Potts superiorization of the conjugate gradients method (CG). More precisely, the CG iterates were perturbed w.r.t. the (block-wise) Potts prior towards more desirable solutions. We have shown that one obtains non-ascending directions w.r.t. the block-wise Potts prior when taking steps towards its proximal mapping. The corresponding superiorization approach, which perturbs the iterates by adding these non-ascending directions, yielded better results than the non-perturbed CG. Furthermore, we provided theory that ensures termination of the resulting algorithm. In practice, we observed further improved results when we perturbed the iterates with the proximal mapping itself. Based on this observation, we developed a new Potts-based superiorization approach, which we called Potts S-CG. Potts S-CG uses the proximal mapping as before and additionally lets the underlying PWLS problem evolve in the course of the iterations, so that the final result becomes genuinely piecewise constant.

The energy minimization approach (Potts ADMM) and the superiorization approach (Potts S-CG) both produce solutions which are (multi-channel) Potts-regularized. We identified Potts ADMM and Potts S-CG as suitable choices within their respective class of methods by comparing them to a penalty method and a method which Potts-superiorizes the Landweber iteration, respectively. Despite the different abstract interpretations, the iterations in Potts ADMM as well as Potts S-CG involve a data step and a regularizing step. The latter decomposes into univariate Potts problems (solved efficiently by dynamic programming). A significant difference between Potts ADMM and Potts S-CG is that the data step of Potts ADMM corresponds to solving an  $\ell_2$ -regularized problem, while the data step of Potts S-CG corresponds to a single CG step.

In our numerical experiments, we applied Potts ADMM and Potts S-CG to simulated multi-spectral CT data and compared them to the existing TV-based methods. Our Potts prior based methods produced sharper edges and mostly higher MSSIM values than TV-type methods. We attribute a large extend of these improvements to the channel-coupling promoted by the multi-channel Potts prior.

## Acknowledgements

We thank J. S. Jørgensen (Technical University of Denmark) for simulation code and D. Kazantsev (Diamond Light Source, UK) for his advice on the provided Github code. L. Kiefer and A. Weinmann were supported by the German Research Foundation (DFG) Grant WE5886/4-1. M. Storath was supported by DFG Grant STO1126/2-1.

## Appendix

### Appendix A.1. Derivation of the ADMM subproblems (21)-(22).

In each iteration, we minimize the Lagrangian  $\mathcal{L}$  as given in (20) w.r.t.  $v$  and  $u_1, \dots, u_S$ . To simplify the expressions for  $\operatorname{argmin}_v \mathcal{L}$  and  $\operatorname{argmin}_{u_s} \mathcal{L}$ , we will use repeatedly the fact that

$$\sum_{i=1}^n x_i(p-t)^2 = \left( \sum_{i=1}^n x_i \right) \left( p - \frac{\sum_{i=1}^N t_i x_i}{\sum_{i=1}^n x_i} \right)^2 + K \quad (\text{A.1})$$

holds for  $p, t_1, \dots, t_n \in \mathbb{R}$  and  $x_1, \dots, x_n > 0$  and a constant  $K$  that does not depend on  $p$ ; see, e.g., [73]. After dropping the terms that do not depend on  $v$ , the subproblem w.r.t.  $v$  reads

$$\operatorname{argmin}_v \sum_{c=1}^C \mathcal{D}(Av_c, f_c) + \sum_{s=1}^S \frac{\rho}{2} \|v - u_s + \frac{\tau_s}{\rho}\|^2. \quad (\text{A.2})$$

Applying (A.1) to (A.2) yields exactly the subproblem in  $v$  as formulated in (21). The subproblem w.r.t.  $u_s$  (again, after dropping terms that do not depend on  $u_s$ ) is given by

$$\operatorname{argmin}_{u_s} \gamma \omega_s \|\nabla_{d_s} u_s\|_0 + \frac{\rho}{2} \|v - u_s + \frac{\tau_s}{\rho}\|^2 + \sum_{r=1}^{s-1} \|u_s - u_r - \frac{\lambda_{r,s}}{\mu}\|^2 + \sum_{t=s+1}^S \|u_s - u_t + \frac{\lambda_{s,t}}{\mu}\|^2. \quad (\text{A.3})$$

After applying (A.1) to (A.3), we obtain

$$\begin{aligned} \operatorname{argmin}_{u_s} \gamma \omega_s \|\nabla_{d_s} u_s\|_0 + \frac{\rho}{2} \|v - u_s + \frac{\tau_s}{\rho}\|^2 \\ + \frac{(s-1)\mu}{2} \left\| u_s - \frac{\sum_{r=1}^{s-1} (u_r + \frac{\lambda_{r,s}}{\mu})}{s-1} \right\|^2 + \frac{(S-s)\mu}{2} \left\| u_s - \frac{\sum_{t=s+1}^S (u_t - \frac{\lambda_{s,t}}{\mu})}{S-s} \right\|^2. \end{aligned} \quad (\text{A.4})$$

We use again (A.1), which yields

$$\operatorname{argmin}_{u_s} \gamma \omega_s \|\nabla_{d_s} u_s\|_0 + \frac{\rho}{2} \|v - u_s + \frac{\tau_s}{\rho}\|^2 + \frac{(s-1)\mu}{2} \left\| u_s - \frac{\sum_{r=1}^{s-1} (u_r + \frac{\lambda_{r,s}}{\mu}) + \sum_{t=s+1}^S (u_t - \frac{\lambda_{s,t}}{\mu})}{S-1} \right\|^2. \quad (\text{A.5})$$

A final application of (A.1) leads to

$$\operatorname{argmin}_{u_s} \gamma \omega_s \|\nabla_{d_s} u_s\|_0 + \frac{\rho+(S-1)\mu}{2} \left\| u_s - \frac{\rho v + \tau_s + \sum_{r=1}^{s-1} (u_r + \frac{\lambda_{r,s}}{\mu}) + \sum_{t=s+1}^S (u_t - \frac{\lambda_{s,t}}{\mu})}{S-1} \right\|^2 \quad (\text{A.6})$$

and multiplying (A.6) by  $\frac{2}{\rho+(S-1)\mu}$  yields subproblem (22).

### Appendix A.2. Conjugate gradient step for a generic least squares problem.

In Algorithm A.1, we provide the pseudocode of an iteration of the conjugate gradient method applied to the normal equations of a generic least squares problem  $\|Bx - b\|^2$  (cf. [89, Alg. 8]).

---

#### Algorithm A.1: CG step for a least squares problem

---

**Input:** System matrix  $B$ , current iterate  $x$ , current auxiliary vectors  $p, h$

**Output:** Updated  $x, p, h$

- 1  $r \leftarrow B^T(Bx - b)$
  - 2  $\alpha = \langle r, h \rangle / \langle p, h \rangle$
  - 3  $p \leftarrow -r + \alpha p$
  - 4  $h \leftarrow B^T B p$
  - 5  $\kappa = -\langle r, p \rangle / \langle p, h \rangle$
  - 6  $x \leftarrow x + \kappa p$
-

## Appendix A.3. Conjugate gradient step for the augmented PWLS problem (45)

In Algorithm A.2, we provide the pseudocode of a step of the CG method applied to the normal equations corresponding to the augmented PWLS problem (45).

**Algorithm A.2:** CG step for the augmented weighted least squares problem (45)

**Input:** Forward operator  $A$ , multispectral sinogram  $f$ , weights  $W_c$ , coupling parameter  $\mu$ , current iterates  $u, p, h$

**Output:** Updated iterates  $u, p, h$

---

```

1 for  $c = 1, \dots, C$  do
2    $r_{s,c} \leftarrow A^T W_c A u_{s,c} - A^T W_c f_c + \sum_{t \neq s} \mu^2 (u_{s,c} - u_{t,c})$  for all  $s = 1, \dots, S$ ,
3    $\alpha = \frac{\sum_s (r_{s,c})^T h_{s,c}}{\sum_s (p_{s,c})^T h_{s,c}}$ ,
4    $p_{s,c} \leftarrow -r_{s,c} + \alpha p_{s,c}$  for all  $s = 1, \dots, S$ ,
5    $h_{s,c} \leftarrow A^T W_c A p_{s,c} + \sum_{t \neq s} \mu^2 (p_{s,c} - p_{t,c})$  for all  $s = 1, \dots, S$ ,
6    $\kappa = -\frac{\sum_s (r_{s,c})^T p_{s,c}}{\sum_s (p_{s,c})^T h_{s,c}}$ ,
7    $u_{s,c} \leftarrow u_{s,c} + \kappa p_{s,c}$  for all  $s = 1, \dots, S$ 
8 end

```

---

## Appendix A.4. Proofs

We here provide the proofs of Lemma 5.2, Lemma 5.3 and Proposition 5.5.

*Proof of Lemma 5.2.* We note that the statement follows from the analogous statement for the univariate Potts problem as the proximal mapping of the block-wise Potts prior corresponds to row- and column-wise univariate Potts problems (as discussed below (35)). For the univariate Potts problem, the statement was proven in [84, Lemma 4.2].  $\square$

*Proof of Lemma 5.3.* The proof essentially follows from Lemma 5.2: starting from  $u = (u_1, u_2)$ , no additional jumps will be opened in  $u + t \cdot v$  for any  $t \geq 0$  as  $v_1$  is constant on the (discrete) row intervals of constant value of  $u_1$  and  $v_2$  on the (discrete) column intervals of constant value of  $u_2$ . Consequently,  $F(u + t \cdot v) \leq F(u)$  for all  $t \geq 0$  which completes the proof.  $\square$

*Proof of Proposition 5.5.* (i) Let  $u^*$  be a minimizer of (41) and define  $(v_1, \dots, v_S) = (u^*, \dots, u^*)$ . We show that  $(v_1, \dots, v_S)$  satisfies the normal equations (45) which is sufficient for a minimizer of (43). It holds by definition that  $v_s = v_t$  for all  $s, t$ . As  $u^*$  satisfies the normal equations of (41), we further obtain  $A^T W A v_{s,c} = A^T W f_c$  for all channels  $c = 1, \dots, C$ . Together,  $(v_1, \dots, v_S)$  satisfies (45) for all channels  $c = 1, \dots, C$ . (ii) We show that the equality of the block variables  $u_s^*$  of a minimizer follows from optimality. To this end, let  $(u_1^*, \dots, u_S^*)$  be a minimizer of (43). Towards a contradiction, we assume that there are  $s \neq t$  such that  $u_s^* \neq u_t^*$  which in particular means  $\sum_{s=1}^S \sum_{t=s+1}^S \frac{1}{2} \|u_{s,c}^* - u_{t,c}^*\| > 0$  for at least one channel  $c$ . For  $(v_1, \dots, v_S) := (u^*, \dots, u^*)$  as above we have that  $\sum_{s=1}^S \frac{1}{2} \|W^{\frac{1}{2}} A v_c^* - W^{\frac{1}{2}} f_c\|^2$  is minimal for each  $c$  in view of  $u^*$  being a minimizer of (41). Further, by definition the quadratic deviations between the block variables vanish, i.e.,  $\sum_{s=1}^S \sum_{t=s+1}^S \frac{1}{2} \|v_{s,c} - v_{t,c}\|^2 = 0$  for all  $c$ . As the sum of these two terms corresponds to the objective in (43),  $(v_1, \dots, v_S)$  yields a lower objective value than  $(u_1^*, \dots, u_S^*)$  which is a contradiction, so  $u_1^* = \dots = u_S^*$ . From the normal equations (44) follows immediately  $A^T W A u_{1,c}^* = A^T W f_c$  for all  $c$  which corresponds to the normal equations of (41). (iii) The third assertion follows from (i) and (ii) together with the uniqueness of least squares problems for full-rank matrices.  $\square$

## References

- [1] L. Ambrosio and V. Tortorelli. Approximation of functional depending on jumps by elliptic functional via  $\Gamma$ -convergence. *Communications on Pure and Applied Mathematics*, 43(8):999–1036, 1990.
- [2] P. Arbelaez, M. Maire, C. Fowlkes, and J. Malik. Contour detection and hierarchical image segmentation. *IEEE Transactions on Pattern Analysis and Machine Intelligence*, 33(5):898–916, 2010.
- [3] I. Auger and C. Lawrence. Algorithms for the optimal identification of segment neighborhoods. *Bulletin of Mathematical Biology*, 51(1):39–54, 1989.
- [4] L. Bar, N. Sochen, and N. Kiryati. Variational pairing of image segmentation and blind restoration. In *ECCV 2004*, pages 166–177. Springer, 2004.
- [5] C. Bargetz, S. Reich, and R. Zalas. Convergence Properties of Dynamic String-Averaging Projection Methods in the Presence of Perturbations. *Numer. Algorithms*, 77:185–209, 2018.
- [6] I. Bayram and M. Kamasak. A directional total variation. In *2012 Proceedings of the 20th European Signal Processing Conference (EUSIPCO)*, pages 265–269. IEEE, 2012.
- [7] A. Beck and M. Teboulle. A fast iterative shrinkage-thresholding algorithm for linear inverse problems. *SIAM Journal on Imaging Sciences*, 2(1):183–202, 2009.
- [8] R. Bellman and R. Roth. Curve fitting by segmented straight lines. *Journal of the American Statistical Association*, 64(327):1079–1084, 1969.
- [9] A. Blake. Comparison of the efficiency of deterministic and stochastic algorithms for visual reconstruction. *IEEE Transactions on Pattern Analysis and Machine Intelligence*, 11(1):2–12, 1989.
- [10] S. Boyd, N. Parikh, E. Chu, B. Peleato, and J. Eckstein. Distributed optimization and statistical learning via the alternating direction method of multipliers. *Foundations and Trends in Machine Learning*, 3(1):1–122, 2011.
- [11] Y. Boykov and V. Kolmogorov. Computing geodesics and minimal surfaces via graph cuts. In *Proceedings Ninth IEEE International Conference on Computer Vision*, pages 26–33, 2003.
- [12] Y. Boykov, O. Veksler, and R. Zabih. Fast approximate energy minimization via graph cuts. *IEEE Transactions on Pattern Analysis and Machine Intelligence*, 23(11):1222–1239, 2001.
- [13] D. Butnariu, R. Davidi, G. T. Herman, and I. G. Kazantsev. Stable Convergence Behavior under Summable Perturbations of a Class of Projection Methods for Convex Feasibility and Optimization Problems. *IEEE J. Sel. Topics Signal Process.*, 1:540–547, 2007.
- [14] D. Butnariu, S. Reich, and A. J. Zaslavski. Convergence to Fixed Points of Inexact Orbits of Bregman-Monotone and of Nonexpansive Operators in Banach Spaces. In H. F. Nathansky, B.G. de Buen, K. Goebel, W. A. Kirk, and B. Sims, editors, *Fixed Point Theory and its Applications*, pages 11 – 32. Yokohama Publ., 2006.
- [15] D. Butnariu, S. Reich, and A. J. Zaslavski. Stable Convergence Theorems for Infinite Products and Powers of Nonexpansive Mappings. *Numer. Func. Anal. Opt.*, pages 304–323, 2008.
- [16] C. Byrne. What do simulations tell us about superiorization? *Preprint. Available on ResearchGate at: [https://www.researchgate.net/publication/336361338\\_What\\_Do\\_Simulations\\_Tell\\_Us\\_About\\_Superiorization\\_revised-October](https://www.researchgate.net/publication/336361338_What_Do_Simulations_Tell_Us_About_Superiorization_revised-October)*, 8, 2019.
- [17] Y. Censor. Superiorization and perturbation resilience of algorithms: a continuously updated bibliography. *arXiv:1506.04219*, 2015.
- [18] Y. Censor, E. Garduño, E. Helou, and G. Herman. Derivative-free superiorization: Principle and algorithm. *Numerical Algorithms*, pages 1–22, 2020.
- [19] Y. Censor, G. T. Herman, and M. Jiang (Editors). *Special Issue on Superiorization: Theory and Applications*, volume 33 (4). IOP Science, Inverse Probl., 2017.
- [20] Y. Censor and E. Levy. An Analysis of the Superiorization Method via the Principle of Concentration of Measure. *Applied Mathematics and Computation*, accepted for publication, 2019.
- [21] Y. Censor, S. Petra, and C. Schnörr. Superiorization vs. accelerated convex optimization: The superiorized/regularized least squares case. *Journal of Applied and Numerical Optimization*, 2(1):15–62, 2020.
- [22] Y. Censor and A. J. Zaslavski. Strict Fejér Monotonicity by Superiorization of Feasibility-Seeking Projection Methods. *J. Optim. Theory Appl.*, 165:172–187, 2015.
- [23] A. Chambolle. Image segmentation by variational methods: Mumford and Shah functional and the discrete approximations. *SIAM Journal on Applied Mathematics*, 55(3):827–863, 1995.
- [24] A. Chambolle. Finite-differences discretizations of the Mumford-Shah functional. *ESAIM: Mathematical Modelling and Numerical Analysis*, 33(02):261–288, 1999.
- [25] A. Chambolle, D. Cremers, and T. Pock. A convex approach to minimal partitions. *SIAM Journal on Imaging Sciences*, 5(4):1113–1158, 2012.
- [26] T. Chan and L. Vese. Active contours without edges. *IEEE Transactions on Image Processing*, 10(2):266–277, 2001.
- [27] R. Chartrand. Exact reconstruction of sparse signals via nonconvex minimization. *IEEE Signal Processing*

- Letters*, 14(10):707–710, 2007.
- [28] R. Chartrand. Fast algorithms for nonconvex compressive sensing: MRI reconstruction from very few data. In *IEEE International Symposium on Biomedical Imaging: From Nano to Macro*, pages 262–265, 2009.
  - [29] R. Chartrand and B. Wohlberg. A nonconvex ADMM algorithm for group sparsity with sparse groups. In *IEEE International Conference on Acoustics, Speech and Signal Processing*, pages 6009–6013, 2013.
  - [30] R. Davidi, G. Herman, and Y. Censor. Perturbation-resilient block-iterative projection methods with application to image reconstruction from projections. *International Transactions in Operational Research*, 16(4):505–524, 2009.
  - [31] Q. Ding, T. Niu, X. Zhang, and Y. Long. Image-domain multimaterial decomposition for dual-energy CT based on prior information of material images. *Medical physics*, 45(8):3614–3626, 2018.
  - [32] N. Ducros, J. Abascal, B. Sixou, S. Rit, and F. Peyrin. Regularization of nonlinear decomposition of spectral X-ray projection images. *Medical physics*, 44(9):e174–e187, 2017.
  - [33] M. Fornasier, R. March, and F. Solombrino. Existence of minimizers of the Mumford-Shah functional with singular operators and unbounded data. *Annali di Matematica Pura ed Applicata*, 192(3):361–391, 2013.
  - [34] M. Fornasier and R. Ward. Iterative thresholding meets free-discontinuity problems. *Foundations of Computational Mathematics*, 10(5):527–567, 2010.
  - [35] F. Friedrich, A. Kempe, V. Liebscher, and G. Winkler. Complexity penalized M-estimation. *Journal of Computational and Graphical Statistics*, 17(1):201–224, 2008.
  - [36] H. Gao, H. Yu, S. Osher, and G. Wang. Multi-energy CT based on a prior rank, intensity and sparsity model (PRISM). *Inverse problems*, 27(11):115012, 2011.
  - [37] S. Geman and D. Geman. Stochastic relaxation, Gibbs distributions, and the Bayesian restoration of images. *IEEE Transactions on Pattern Analysis and Machine Intelligence*, 6:721–741, 1984.
  - [38] T. Goldstein and S. Osher. The split Bregman method for L1-regularized problems. *SIAM Journal on Imaging Sciences*, 2(2):323–343, 2009.
  - [39] B. Gonzales and D. Lalush. Full-spectrum CT reconstruction using a weighted least squares algorithm with an energy-axis penalty. *IEEE Transactions on Medical Imaging*, 30(2):173–183, 2010.
  - [40] E. Helou, G. Herman, C. Lin, and M. Zibetti. Superiorization of preconditioned conjugate gradient algorithms for tomographic image reconstruction. *arXiv:1807.10151*, 2018.
  - [41] G. Herman, E. Garduño, R. Davidi, and Y. Censor. Superiorization: An optimization heuristic for medical physics. *Medical physics*, 39(9):5532–5546, 2012.
  - [42] K. Hohm, M. Storath, and A. Weinmann. An algorithmic framework for Mumford–Shah regularization of inverse problems in imaging. *Inverse Problems*, 31(11):115011, 2015.
  - [43] M. Hong, Z.-Q. Luo, and M. Razaviyayn. Convergence analysis of alternating direction method of multipliers for a family of nonconvex problems. *SIAM Journal on Optimization*, 26(1):337–364, 2016.
  - [44] B. Jackson, J. Scargle, D. Barnes, S. Arabhi, A. Alt, P. Gioumoussis, E. Gwin, P. Sangtrakulcharoen, L. Tan, and T. Tsai. An algorithm for optimal partitioning of data on an interval. *IEEE Signal Processing Letters*, 12(2):105–108, 2005.
  - [45] M. Jiang, P. Maass, and T. Page. Regularizing properties of the Mumford-Shah functional for imaging applications. *Inverse Problems*, 30(3):035007, 2014.
  - [46] D. Kazantsev, J. Jørgensen, M. Andersen, W. Lionheart, P. Lee, and P. Withers. Joint image reconstruction method with correlative multi-channel prior for X-ray spectral computed tomography. *Inverse Problems*, 34(6):064001, 2018.
  - [47] L. Kiefer and S. Petra. Performance bounds for cosparsity multichannel signal recovery via collaborative-TV. In *International Conference on Scale Space and Variational Methods in Computer Vision*, pages 295–307, 2017.
  - [48] L. Kiefer, M. Storath, and A. Weinmann. Iterative Potts minimization for the recovery of signals with discontinuities from indirect measurements: the multivariate case. *Foundations of Computational Mathematics*, 2020.
  - [49] J. Kim, A. Tsai, M. Cetin, and A. Willsky. A curve evolution-based variational approach to simultaneous image restoration and segmentation. In *Proceedings of the IEEE International Conference on Image Processing*, volume 1, pages I–109. IEEE, 2002.
  - [50] E. Klann. A Mumford-Shah-like method for limited data tomography with an application to electron tomography. *SIAM Journal on Imaging Sciences*, 4(4):1029–1048, 2011.
  - [51] E. Klann and R. Ramlau. Regularization properties of Mumford-Shah-type functionals with perimeter and norm constraints for linear ill-posed problems. *SIAM Journal on Imaging Sciences*, 6(1):413–436, 2013.
  - [52] E. Klann, R. Ramlau, and W. Ring. A Mumford-Shah level-set approach for the inversion and segmentation of SPECT/CT data. *Inverse Problems and Imaging*, 5(1):137–166, 2011.
  - [53] G. Li and T. Pong. Global convergence of splitting methods for nonconvex composite optimization. *SIAM Journal on Optimization*, 25(4):2434–2460, 2015.
  - [54] Y. Long and J. Fessler. Multi-material decomposition using statistical image reconstruction for spectral CT. *IEEE Trans Med Imaging*, 33(8):1614–1626, 2014.

- [55] D. Mumford and J. Shah. Optimal approximations by piecewise smooth functions and associated variational problems. *Communications on Pure and Applied Mathematics*, 42(5):577–685, 1989.
- [56] M. Ng, P. Weiss, and X. Yuan. Solving constrained total-variation image restoration and reconstruction problems via alternating direction methods. *SIAM Journal on Scientific Computing*, 32(5):2710–2736, 2010.
- [57] T. Pock, A. Chambolle, D. Cremers, and H. Bischof. A convex relaxation approach for computing minimal partitions. In *IEEE Conference on Computer Vision and Pattern Recognition*, pages 810–817, 2009.
- [58] R. Potts. Some generalized order-disorder transformations. *Mathematical Proceedings of the Cambridge Philosophical Society*, 48:106–109, 1 1952.
- [59] R. Ramlau and W. Ring. A Mumford-Shah level-set approach for the inversion and segmentation of X-ray tomography data. *Journal of Computational Physics*, 221(2):539–557, 2007.
- [60] R. Ramlau and W. Ring. Regularization of ill-posed Mumford–Shah models with perimeter penalization. *Inverse Problems*, 26(11):115001, 2010.
- [61] W. Rand. Objective criteria for the evaluation of clustering methods. *Journal of the American Statistical association*, 66(336):846–850, 1971.
- [62] D. Rigie and P. La Rivière. Joint reconstruction of multi-channel, spectral CT data via constrained total nuclear variation minimization. *Physics in Medicine & Biology*, 60(5):1741, 2015.
- [63] L. Rudin, S. Osher, and E. Fatemi. Nonlinear total variation based noise removal algorithms. *Physica D: Nonlinear Phenomena*, 60(1):259–268, 1992.
- [64] K. Sauer and C. Bouman. A local update strategy for iterative reconstruction from projections. *IEEE Transactions on Signal Processing*, 41(2):534–548, 1993.
- [65] O. Semerci, N. Hao, M. Kilmer, and E. Miller. Tensor-based formulation and nuclear norm regularization for multienergy computed tomography. *IEEE Trans. Image Processing*, 23(4):1678–1693, 2014.
- [66] L. Shepp and Y. Vardi. Maximum likelihood reconstruction for emission tomography. *IEEE transactions on medical imaging*, 1(2):113–122, 1982.
- [67] P. Shikhaliev. Energy-resolved computed tomography: first experimental results. *Physics in Medicine & Biology*, 53(20):5595, 2008.
- [68] J. Siewerdsen, A. Waese, D. Moseley, S. Richard, and D. Jaffray. Spektr: A computational tool for X-ray spectral analysis and imaging system optimization. *Medical physics*, 31(11):3057–3067, 2004.
- [69] G. Steidl and T. Teuber. Removing multiplicative noise by Douglas-Rachford splitting methods. *Journal of Mathematical Imaging and Vision*, 36(2):168–184, 2010.
- [70] M. Storath, L. Kiefer, and A. Weinmann. Smoothing for signals with discontinuities using higher order Mumford–Shah models. *Numerische Mathematik*, 143(2):423–460, 2019.
- [71] M. Storath and A. Weinmann. Fast partitioning of vector-valued images. *SIAM Journal on Imaging Sciences*, 7(3):1826–1852, 2014.
- [72] M. Storath, A. Weinmann, and L. Demaret. Jump-sparse and sparse recovery using Potts functionals. *IEEE Transactions on Signal Processing*, 62(14):3654–3666, 2014.
- [73] M. Storath, A. Weinmann, J. Friel, and M. Unser. Joint image reconstruction and segmentation using the Potts model. *Inverse Problems*, 31(2):025003, 2015.
- [74] J. Toivanen, A. Meaney, S. Siltanen, and V. Kolehmainen. Joint reconstruction in low dose multi-energy CT. *Inverse problems and Imaging*, 14(4):607–629, 2020.
- [75] J. Tuszynski. 2006-2016 PhotonAttenuation–Software for modeling of photons passing through different materials. <https://uk.mathworks.com/matlabcentral/fileexchange/12092-photonattenuation>.
- [76] W. Van Aarle, W. Palenstijn, J. De Beenhouwer, T. Altantzis, S. Bals, J. Batenburg, and J. Sijbers. The ASTRA toolbox: A platform for advanced algorithm development in electron tomography. *Ultramicroscopy*, 157:35–47, 2015.
- [77] O. Veksler. *Efficient graph-based energy minimization methods in computer vision*. PhD thesis, Cornell University, 1999.
- [78] F. Wang, W. Cao, and Z. Xu. Convergence of multi-block Bregman ADMM for nonconvex composite problems. *Science China Information Sciences*, 61(12):122101, 2018.
- [79] F. Wang, Z. Xu, and H.-K. Xu. Convergence of Bregman alternating direction method with multipliers for nonconvex composite problems. *arXiv:1410.8625*, 2014.
- [80] Y. Wang, W. Yin, and J. Zeng. Global convergence of ADMM in nonconvex nonsmooth optimization. *Journal of Scientific Computing*, 78(1):29–63, 2019.
- [81] Z. Wang, A. Bovik, H. Sheikh, and E. Simoncelli. Image quality assessment: from error visibility to structural similarity. *IEEE Transactions on Image Processing*, 13(4):600–612, 2004.
- [82] A. Weinmann and M. Storath. Iterative Potts and Blake–Zisserman minimization for the recovery of functions with discontinuities from indirect measurements. *Proc. R. Soc. A*, 471(2176):20140638, 2015.
- [83] Z. Wen, C. Yang, X. Liu, and S. Marchesini. Alternating direction methods for classical and ptychographic phase retrieval. *Inverse Problems*, 28(11):115010, 2012.
- [84] G. Winkler and V. Liebscher. Smoothers for discontinuous signals. *Journal of Nonparametric Statistics*, 14(1-2):203–222, 2002.



- [85] O. Wittich, A. Kempe, G. Winkler, and V. Liebscher. Complexity penalized least squares estimators: Analytical results. *Mathematische Nachrichten*, 281(4):582–595, 2008.
- [86] Z. Xu, S. De, M. Figueiredo, C. Studer, and T. Goldstein. An empirical study of ADMM for nonconvex problems. *arXiv:1612.03349*, 2016.
- [87] J. Yang and Y. Zhang. Alternating direction algorithms for  $\ell_1$ -problems in compressive sensing. *SIAM Journal on Scientific Computing*, 33(1):250–278, 2011.
- [88] L. Yang, T. Pong, and X. Chen. Alternating direction method of multipliers for a class of nonconvex and nonsmooth problems with applications to background/foreground extraction. *SIAM Journal on Imaging Sciences*, 10(1):74–110, 2017.
- [89] M. Zibetti, C. Lin, and G. Herman. Total variation superiorized conjugate gradient method for image reconstruction. *Inverse Problems*, 34(3):034001, 2018.